



Master's Thesis

Université Paris-Saclay - Mathématiques et Applications
Analyse, Modélisation, Simulation

Launch Pad Noise Reduction using Metamaterial Structures

Author
Philippe MARCHNER

Supervisors ESA-ESTEC
Ivan NGAN
Graham COE

Supervisor PARIS-SACLAY
Laurent DUMAS

Mechanical Departement - Structures Section (TEC-MSS)
European Space Research and Technology Center
Keplerlaan 1, 2201 AZ Noordwijk, The Netherlands
September 7, 2018

Abstract

During rocket launch, the intense and complex acoustic environment induces vibrations on the payload fairing and might cause the spatial mission to fail. This report studies the possibility to mitigate the noise during the launch by using a metastructure as an add-on to the launch pad. More specifically, the present work investigates different types of Helmholtz problems in sonic crystals.

Numerical tools are developed to analyze their acoustic properties such as band gaps, diffraction gratings or local resonances. In two dimensions, finite element simulations examines the nature of acoustic waves in infinite and finite sonic crystals. The results provide early stage design rules to tailor the properties of sonic crystals for a large scale application: the acoustic scattering of the Vega launch pad.

In three dimensions, boundary element formulations are combined with high performance computing tools. The acoustic field is computed during the ignition and lift-off phases of Vega, where the far field response is recorded at the fairing location. It is found that compared to a classic trench covering, sonic crystals peculiar properties could be efficiently tuned towards a more efficient noise reduction. The limitations of the physical model and numerical issues are highlighted.

Keywords: Sonic crystal, launch pad, Vega, Helmholtz problem, FEM, BEM, band gap, diffraction.

Contents

1	Introduction	1
1.1	Acoustic environment of launchers	1
1.2	Metamaterial structure for the launch pad	2
1.3	Organization of the report	3
2	Sound propagation in Sonic Crystals	5
2.1	Physical framework	5
2.1.1	Acoustic equations	5
2.1.2	Periodic media	6
2.1.3	Practical examples	8
2.2	One dimensional medium	9
2.2.1	Infinite medium	9
2.2.2	Finite size medium	11
2.3	Two dimensional sonic crystal	12
2.3.1	Band structure of an infinite crystal	13
2.3.2	Transmission loss of a 1-direction finite sonic crystal	17
2.3.3	Finite sonic crystal in 2-directions	20
3	Preliminary development on the Launch Pad	23
3.1	Boundary Element formulations	23
3.1.1	Helmholtz problem and representation formula	23
3.1.2	Trace operators and Boundary Integral Equations	25
3.2	Discretization, system preconditioning and fast algorithms	27
3.3	Scattering of a sound-hard sphere	28
3.4	Scattering of a cylindrical array of scatterers	30
3.5	Scattering of the Vega launch pad	31
3.5.1	Solving strategy	32
3.5.2	Sonic crystals: insertion loss for the launch pad	33
3.5.3	Additional remarks	36
Conclusion		37
A	Illustrations of the Vega launcher	39
B	Locally resonant sonic crystal	41
C	Difficulties for 3D accelerated boundary element method	45
C.1	High frequency limit	45
C.2	Multiple scattering	45
C.3	Position of the source	47
C.4	Additional remarks	47

Chapter 1

Introduction

1.1 Acoustic environment of launchers

During ignition and lift-off, launch vehicles are subjected to intense mechanical vibrations which can badly damage the spacecraft and put at risk the spatial mission.

The intense acoustic field generated by the rocket engine is the main cause of these vibrations. The acoustic source is transient and has a high amplitude with a complex spectrum. It is induced by the exhaust plume flow which emits blast waves and a high temperature supersonic jet. For rocket engines, the radiated acoustic power scales with the fifth power of the jet velocity. A simplified situation is presented in figure (1.1). The acoustic field then impinges the launch pad and reflects back to excite the fairing, where the sound is transmitted onto the payload.

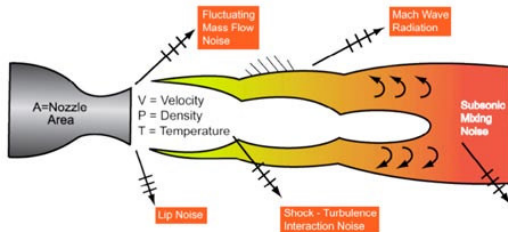


Figure 1.1: Noise sources from a supersonic jet. Extracted figure from [1].

Strict acoustic specifications have been set up to prevent damage to the payload. Figure (1.2) shows the measured acoustic load envelope under the fairing for the Vega and Ariane 5 launchers. Before the flight mission, the payload must withstand a diffuse field of 3 dB over the measurements during 120 seconds. The tests can be conducted in the Large European Acoustic Facility (LEAF) at ESTEC or in other facilities over the world. The ESTEC reverberation room can produce a broadband acoustic spectrum up to 156 dB amplitude [2]. Large lightweight structures such as solar arrays are particularly sensitive to acoustic loads. If the payload is composed of such structures, independent vibro-acoustic analysis needs to be carried out.

Noise and vibration reduction technologies can highly increase the sustainability of future missions. Both passive and active noise control techniques are important fields of research. The present study focuses on passive acoustic technologies. The underlying idea is to locally modify the sound field in order to mitigate the noise without external energy addition.

One strategy is to design an acoustic treatment to protect the fairing. On Ariane 5, acoustic

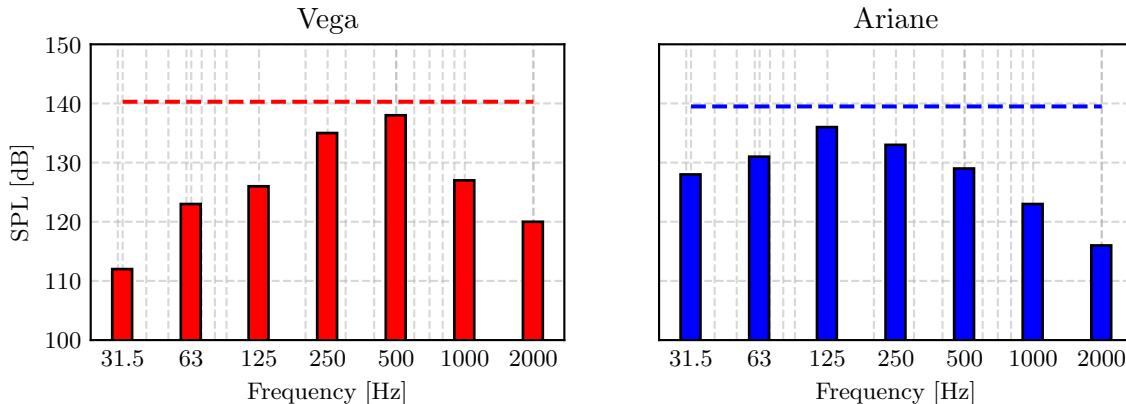


Figure 1.2: Measured Sound Pressure Level under the fairing per octave bands for Vega and Ariane 5 launchers during flight. Dashed lines represent the Overall Sound Pressure Level. Extracted data from [3] and [4].

absorbers have been successfully installed [5]. It consists in Helmholtz resonators coupled with foam. Recent models have been developed to design a novel poro-elastic core by coupling a thin layer of fabric with the acoustic absorption of a porous layer [6]. However, the fairing is limited by mass and space constraints.

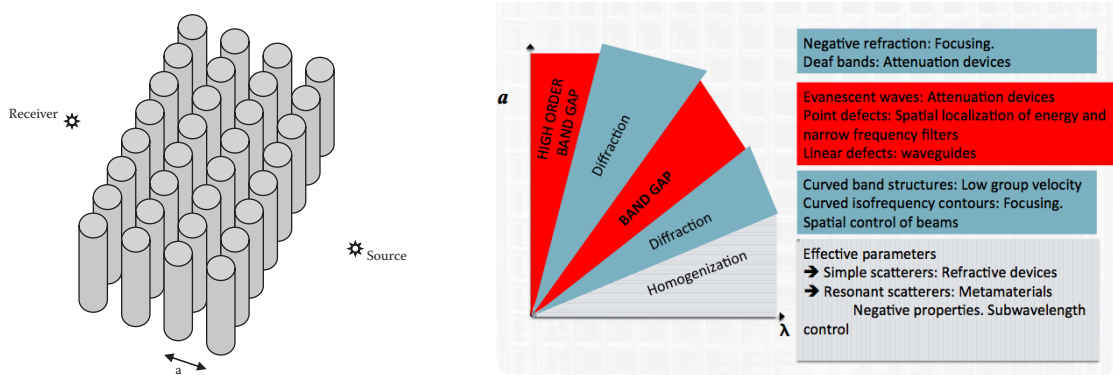
Another strategy is to reduce the noise at the source. The Japan Aerospace Exploration Agency (JAXA) investigated shape optimization of the flame deflector by the mean of Large-eddy simulation (LES) [7]. Water deluge has shown to be an efficient technique, especially when water is injected next to the rocket plume. A proper air water mixing helps to reduce the amount of turbulent kinetic energy from the rocket flow and hence the reflected noise [8]. Kandula [9] suggests that there exists an optimal mass flow rate of water injection for broadband shock noise reduction. On Ariane 5, the launch pad trenches have been covered and a significant improvement in sound attenuation has been reported for low altitudes [10]. However, the hard covering trenches might create additional acoustic reflections during lift-off.

1.2 Metamaterial structure for the launch pad

This study proposes to design a material as an add-on to the launch pad. Conventional materials like foams or perforated plates are not suited to the extreme launch conditions. The concept of a metamaterial structure is investigated as a possible solution to mitigate noise with the possibility to combine it with water deluge. The idea follows the study initiated in 2012 by ESA and the University of Valencia [11], [12]. Metamaterial structures were shown to have good acoustic diffusion properties experimentally and numerically.

The term metamaterial refers to a material whose properties cannot be found in nature. Its peculiar behaviour is the result of its design at a smaller scale. There exists a large literature on the analysis of such materials in quantum physics, electromagnetic or elasticity. The research in acoustic metamaterials started around twenty years ago and has already applications in acoustic cloaking, focusing or negative refraction.

This study investigates the propagation of acoustic waves in materials composed by a periodic repetition of acoustically rigid inclusions in a matrix. This specific metamaterial will be called **sonic crystal**. A typical example is shown in figure (1.3a). The periodic pattern of the



(a) Example of a sonic crystal study configuration. Extracted figure from [13].

(b) Working regimes depending on the ratio between the sonic crystal periodicity a and the acoustic wavelength λ . Extracted figure from [12].

Figure 1.3: Sonic crystal and associated physical phenomena.

crystal gives it specific physical properties. Figure (1.3b) presents an overview of the physical phenomena and regimes that can occur in a sonic crystal. An attempt to analyze these phenomena is done step by step with the help of one, two and three dimensional simulations.

The engineering challenge proposed herein is to design such a sonic crystal and set it up on the Vega launch pad for a simplified, but full scale acoustic simulation. Both ignition and lift-off configurations are studied. The strategy to manipulate the acoustic energy during the rocket launch is the following:

- block the transmission of acoustic waves towards the fairing during ignition,
- spread over time and diffuse the reflected acoustic energy during lift-off.

Additional absorption effects will be considered by the investigation of sonic crystals with local resonances. The objective is then to show a simple proof of concept of the sonic crystal efficiency for the Vega launch pad.

From a practical point of view, the sonic crystal should be installed sufficiently far from the engine exhaust jet. Rigid inclusions are mandatory due to the severe thermal and mechanical conditions in the vicinity of the material. The sonic crystal should also be resistant to water. In short, the goal is to design a rigid material on a large scale in order to manipulate the acoustic energy without modifications of the existent launch pad.

1.3 Organization of the report

The report is organized as follow: the first part will describe the theoretical and numerical tools used for the analysis of acoustic metamaterials. Infinite and finite media will be studied



Figure 1.4: Launch platform of Vega in Kourou, French Guiana. View on the exhaust duct to be covered by a sonic crystal.

in one and two dimensions. The physical effects will be highlighted and compared to other studies. The approach will help to understand and tailor the properties of the material to be used on the launch pad.

In the second part, the acoustic scattering of the launch vehicle will be simulated during ignition and lift-off. A three dimensional boundary element method will be set up and carried out for the acoustic exterior problem. The pressure directivity in the far field will be analyzed to show the potential efficiency of the previously designed metamaterial. The physical model, the integration of the acoustic treatment to a future launch pad and the limitations of the simulation will be discussed.

Specific details will be given on the mathematical formulations derived from the encountered physical problems. It will include finite element discretization, generalized eigenvalue problem, absorbing boundary condition and boundary element formulations for high frequency scattering.

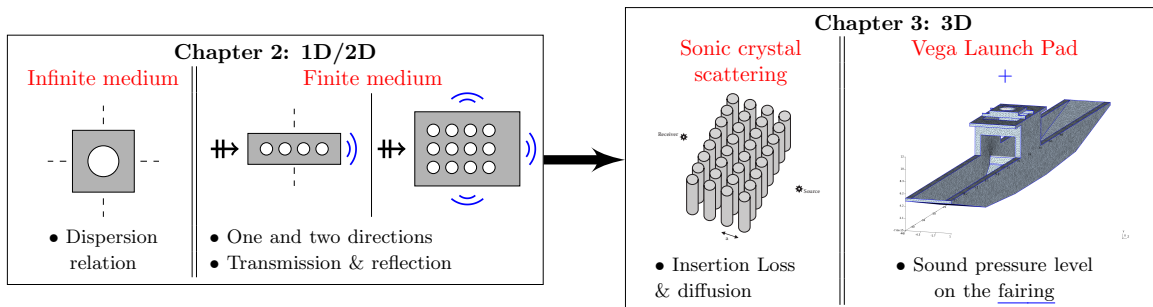


Figure 1.5: Overview of the simulation and modeling work for the application of sonic crystals on the launch pad.

Chapter 2

Sound propagation in Sonic Crystals

This section aims to develop the theoretical tools for the propagation of sound in metamaterials. The acoustic equations and fundamental properties of sonic crystals are first described. Then, the behaviour of sound waves in sonic crystals are studied numerically in one and two dimensions. Band gap structure and acoustic properties are computed for different configurations. All the finite elements computations presented in this section are performed with the open-source FEniCS platform [14, 15, 16].

2.1 Physical framework

The explanations on periodic media have been greatly inspired from Simon Horsley lectures notes and notebooks [17].

2.1.1 Acoustic equations

Sound is a time-space dependent pressure fluctuation. The pressure fluctuations are described by a scalar field $P(\mathbf{x}, t)$, where $t > 0$ is the time and $\mathbf{x} \in \mathbb{R}^3$ the spatial coordinate. Under the assumptions of linear acoustics, the pressure in free space is governed by the wave equation:

$$\Delta P(\mathbf{x}, t) - \frac{1}{c_0^2} \frac{\partial^2 P}{\partial t^2}(\mathbf{x}, t) = F(\mathbf{x}, t), \quad (2.1)$$

where c_0 is the isentropic speed of sound and F an external source. This equation will be studied in the frequency domain. To do so, we define the Fourier transform:

$$\forall \mathbf{x} \in \mathbb{R}^3, \forall t > 0, \quad P(\mathbf{x}, t) = \int_{-\infty}^{+\infty} p(\mathbf{x}, \omega) e^{-i\omega t} d\omega. \quad (2.2)$$

This definition holds for $p \in L^2(\mathbb{R})$. By linearity of the differential operators, the use of the Fourier transform in equation (2.1) leads to the Helmholtz equation:

$$\Delta p(\mathbf{x}, \omega) + \frac{\omega^2}{c_0^2} p(\mathbf{x}, \omega) = f(\mathbf{x}, \omega). \quad (2.3)$$

The $e^{-i\omega t}$ convention has been used in the Fourier transform, which means that radiated waves are traveling outward. For simplicity, we denote $p(\mathbf{x}, \omega)$ by $p(\mathbf{x})$. We also denote $k_0 = \frac{\omega}{c_0}$ the acoustic wavenumber.

As set as above, the Helmholtz formulation is not well-posed. The pressure has to satisfy the so-called Sommerfeld radiation condition. This condition ensures that the energy radiated from the source scatters to infinity. In 3D, it writes:

$$p = \mathcal{O}(1/r), \quad \frac{\partial p}{\partial r} - ik_0 p = \mathcal{O}(1/r^2), \quad \text{as } r \rightarrow \infty, \quad (2.4)$$

where $r = |\mathbf{x} - \mathbf{x}_s|$ is the distance between a field point \mathbf{x} and a source location \mathbf{x}_s . To find a solution of the pressure field in the time-domain, one needs to solve the Helmholtz equation for all the frequencies ω . Then, the real part of the Fourier transform characterizes the physical solution.

In this section, the Helmholtz equation will be solved in a medium composed by a periodic distribution of rigid obstacles. To understand what it implies on the pressure field, an approach by symmetry operators is proposed.

2.1.2 Periodic media

The time-frequency transformation described above can be seen as a continuous symmetry operator: the nature of the pressure field is invariant by any time change of $\delta t > 0$. In other words, both $P(\mathbf{x}, t + \delta t)$ and $P(\mathbf{x}, t)$ are solutions of the same wave equation. It implies that the time translation operator commutes with the wave equation operator. Therefore, they share a common eigenbasis. If we look for the eigenvalues of the time translation operator

$$T_{\delta t} P : P(\mathbf{x}, t) \mapsto P(\mathbf{x}, t + \delta t), \quad (2.5)$$

i.e we look for the non-zero solutions of:

$$P(\mathbf{x}, t + \delta t) = \lambda P(\mathbf{x}, t), \quad \lambda \in \mathbb{C}^*,$$

we find with a first order Taylor expansion that: $P(\mathbf{x}, t) = p(\mathbf{x}, \lambda) e^{\frac{\lambda-1}{\delta t} t} = p(\mathbf{x}, \omega) e^{-i\omega t}$. This corresponds to the harmonic assumption. It means that the set of monochromatic waves are eigenvalues of the wave equation operator and the solutions of the Helmholtz equation are the eigenmodes.

A similar approach can be applied to a discrete symmetry operator. In periodic media, there is a repeating pattern that forms a translation symmetry. This pattern is characterized by the so-called direct lattice. The direct lattice is spanned by the direct vectors \mathbf{a}_1 and \mathbf{a}_2 for a two dimensional medium. They are shown in figure (2.1) for two types of periodicity: rectangular and hexagonal. There exists five types of periodicity in 2D, two of them are studied in the present work. The analysis is restricted to 2D for simplicity. We note the direct lattice by:

$$\mathbf{R} = n\mathbf{a}_1 + m\mathbf{a}_2, \quad (n, m) \in \mathbb{Z}^2. \quad (2.6)$$

The associated discrete translation operator might be written:

$$T_{n,m} p : p(\mathbf{x}) \mapsto p(\mathbf{x} + n\mathbf{a}_1 + m\mathbf{a}_2). \quad (2.7)$$

This operator commutes with the Helmholtz operator ($\Delta + k_0^2$). We can thus look for solutions who are eigenfunctions of the translation operator:

$$p(\mathbf{x} + n\mathbf{a}_1 + m\mathbf{a}_2) = \lambda p(\mathbf{x}), \quad \lambda \in \mathbb{C}^*.$$

We now expand p into a Fourier integral. This results in:

$$\int_{\mathbb{R}^2} \hat{p}(\mathbf{G}) e^{i\mathbf{G} \cdot (\mathbf{x} + \mathbf{R})} d\mathbf{G} = \lambda \int_{\mathbb{R}^2} \hat{p}(\mathbf{G}) e^{i\mathbf{G} \cdot \mathbf{x}} d\mathbf{G}.$$

The equality holds if the quantity $e^{i\mathbf{G} \cdot \mathbf{R}}$ remains constant, which means:

$$\exists (N, C) \in \mathbb{N} \times \mathbb{C}, \quad \mathbf{G} \cdot \mathbf{R} = 2\pi N + C,$$

and the vector \mathbf{G} is decomposed as:

$$\mathbf{G} = \mathbf{K} + \mathbf{k}, \quad \text{with} \quad \begin{cases} \mathbf{k} \cdot \mathbf{R} = & 2\pi N \\ \mathbf{K} \cdot \mathbf{R} = & C \end{cases}.$$

We suppose that \mathbf{k} takes the form $\mathbf{k} = q\mathbf{b}_1 + r\mathbf{b}_2$, so that:

$$\mathbf{k} \cdot \mathbf{R} = (q \quad r) \begin{pmatrix} \mathbf{b}_1 \cdot \mathbf{a}_1 & \mathbf{b}_1 \cdot \mathbf{a}_2 \\ \mathbf{b}_2 \cdot \mathbf{a}_1 & \mathbf{b}_2 \cdot \mathbf{a}_2 \end{pmatrix} \begin{pmatrix} n \\ m \end{pmatrix} = 2\pi N.$$

The vectors \mathbf{b}_1 and \mathbf{b}_2 are chosen such as the following duality relation holds:

$$\mathbf{b}_i \cdot \mathbf{a}_j = 2\pi \delta_{ij}, \quad (2.8)$$

δ_{ij} being the Kronecker symbol. It leads to:

$$nq + mr = N.$$

Since $(m, n) \in \mathbb{Z}^2$, the same must be true for q and r . Hence \mathbf{k} forms a discrete lattice, spanned by \mathbf{b}_1 and \mathbf{b}_2 . It is called the reciprocal lattice. With the duality relation (2.8), we can derive a relation between the direct and reciprocal lattice. If we note $\mathbf{b}_i = \begin{pmatrix} b_{i,x} \\ b_{i,y} \end{pmatrix}$ and $\mathbf{a}_j = \begin{pmatrix} a_{j,x} \\ a_{j,y} \end{pmatrix}$, relation (2.8) becomes:

$$\begin{pmatrix} b_{1,x} & b_{1,y} \\ b_{2,x} & b_{2,y} \end{pmatrix} \begin{pmatrix} a_{1,x} & a_{2,x} \\ a_{1,y} & a_{2,y} \end{pmatrix} = \begin{pmatrix} 2\pi & 0 \\ 0 & 2\pi \end{pmatrix}.$$

It leads to:

$$\mathbf{b}_1 = \frac{2\pi}{a_{1,x}a_{2,y} - a_{1,y}a_{2,x}} \begin{pmatrix} a_{2,y} \\ -a_{1,y} \end{pmatrix}, \quad \mathbf{b}_2 = \frac{2\pi}{a_{1,x}a_{2,y} - a_{1,y}a_{2,x}} \begin{pmatrix} -a_{2,x} \\ a_{1,x} \end{pmatrix}. \quad (2.9)$$

With the fact that $\mathbf{G} = \mathbf{K} + \mathbf{k}$, the pressure field can be interpreted as a sum over multiples of the reciprocal lattice vectors:

$$p(\mathbf{x}) = \int_{\mathbb{R}^2} \widehat{p}(\mathbf{G}) e^{i\mathbf{G} \cdot \mathbf{x}} d\mathbf{G} = e^{i\mathbf{K} \cdot \mathbf{x}} \sum_{q,r} \widehat{p}_{q,r} e^{i\mathbf{k} \cdot \mathbf{x}} = e^{i\mathbf{K} \cdot \mathbf{x}} \widetilde{p}(\mathbf{x}),$$

and $\widetilde{p}(\mathbf{x})$ is a periodic function with the periodicity of the direct lattice:

$$\widetilde{p}(\mathbf{x} + \mathbf{R}) = \widetilde{p}(\mathbf{x}).$$

This is exactly the purpose of Bloch theorem. In a periodic medium, the pressure field equals a periodic function modulated by a phase shift. The vector \mathbf{K} is sometimes referred to Bloch wavenumber and the eigenmode $\widetilde{p}(\mathbf{x})$ to Bloch eigenmode. The vector \mathbf{K} lies in the reciprocal space. The smallest repeating pattern in the reciprocal space is called the First Brillouin Zone. If the vector \mathbf{K} spans all the values in this zone, a solution of the Helmholtz equation can be characterized with the Bloch theorem. Additional geometric symmetry considerations can further reduce this zone into the Irreducible Brillouin Zone (IBZ).

2.1.3 Practical examples

As an example, we consider a periodic media filled with circles for the square and hexagonal periodicity. The corresponding direct basis are given by:

$$\mathbf{a}_1 = a \begin{pmatrix} 1 \\ 0 \end{pmatrix}, \quad \mathbf{a}_2 = a \begin{pmatrix} \cos(\phi) \\ \sin(\phi) \end{pmatrix}, \quad (2.10)$$

with $\phi = \pi/2$ for square periodicity and $\phi = \pi/3$ for hexagonal periodicity. The physical dimension of the unit cell a is called the lattice constant. In this work, we often use $a = 1$. The vectors \mathbf{a}_1 and \mathbf{a}_2 define the unit cell. The unit cell is the smallest repeating pattern in the direct space. From relation (2.9), the reciprocal basis are:

$$\mathbf{b}_1 = \frac{2\pi}{a\sin(\phi)} \begin{pmatrix} \sin(\phi) \\ -\cos(\phi) \end{pmatrix}, \quad \mathbf{b}_2 = \frac{2\pi}{a\sin(\phi)} \begin{pmatrix} 0 \\ 1 \end{pmatrix}. \quad (2.11)$$

The associated Brillouin zones are shown in figure (2.1). Note that in 1D, the unit cell reduces to $[0, a]$ and the first Brillouin zone to $[-\pi/a, \pi/a]$.

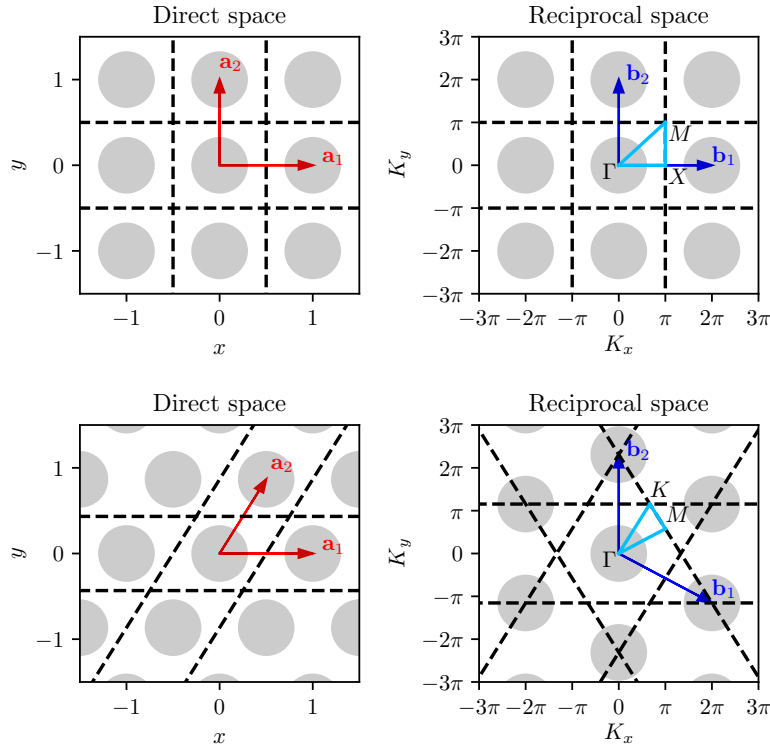


Figure 2.1: Direct and reciprocal space for square (top) and hexagonal (bottom) periodicity with $a = 1$. The first Brillouin zone is the smallest enclosed area by the black dashed lines of the reciprocal space. The Irreducible Brillouin Zone is the enclosed skyblue path: Γ - X - M for square periodicity and Γ - M - K for hexagonal periodicity.

In the next part, we will take advantage of the Bloch theorem to discretize Helmholtz equation in such periodic media. Physical properties of the media are obtained from the analysis.

2.2 One dimensional medium

This section analyzes a one dimensional sonic crystal of infinite and finite size. It allows to understand simple acoustic properties of periodic media. The proposed approach is inspired from [18] and [19].

2.2.1 Infinite medium

A two-layers unit cell is considered, as shown in figure (2.2). The unit cell is repeated infinitely

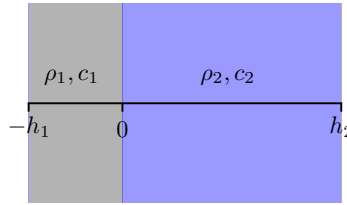


Figure 2.2: Unit cell for an infinite 1D periodic medium. Each layer of the unit cell is characterized by its density ρ and speed of sound c .

along the axis with a periodicity $H = h_1 + h_2$, where H is the width of the unit cell. The 1D Helmholtz equation for the acoustic pressure in the unit cell writes:

$$\frac{d^2 p_i}{dz^2}(z) + k_i^2 p_i(z) = 0, \quad z \in [-h_1, h_2], \quad i \in \{1, 2\}, \quad (2.12)$$

where $k_i = \frac{\omega}{c_i}$ is the wavenumber of medium i and z being the axis coordinate. We consider a solution of the form:

$$\begin{cases} p_1(z) = a_1 \cos(k_1 z) + b_1 \sin(k_1 z) \\ p_2(z) = a_2 \cos(k_2 z) + b_2 \sin(k_2 z) \end{cases}. \quad (2.13)$$

The four unknowns (a_1, b_1, a_2, b_2) have to be determined by boundary conditions. The first condition expresses the continuity of the acoustic pressure and velocity at the interface between the two layers:

$$\begin{cases} p_1(0) = p_2(0) \\ v_1(0) = v_2(0) \end{cases}, \quad (2.14)$$

where the acoustic velocity is related to the acoustic pressure by Euler equation:

$$v_i = -\frac{1}{i\omega\rho_i} \frac{dp_i}{dz}, \quad i \in \{1, 2\}. \quad (2.15)$$

If we denote $Z_i = \rho_i c_i$ the acoustic impedance of medium i and $\gamma = \frac{Z_1}{Z_2}$, equation (2.14) becomes:

$$\begin{cases} a_1 = a_2 \\ b_1 = \gamma b_2 \end{cases}. \quad (2.16)$$

The two other boundary conditions take into account the periodicity of the medium and are given by Bloch theorem. They map the value at $z = h_2$ to the value at $z = -h_1$:

$$\begin{cases} p_2(h_2) = p_1(-h_1)e^{ikH} \\ v_2(h_2) = v_1(-h_1)e^{ikH} \end{cases}. \quad (2.17)$$

These conditions are called Bloch or Floquet-Bloch boundary conditions. The boundary conditions can now be arranged in a matrix form:

$$\begin{pmatrix} 1 & 0 & -1 & 0 \\ 0 & 1 & 0 & -\gamma \\ -e^{ikH}\cos(k_1 h_1) & e^{ikH}\sin(k_1 h_1) & \cos(k_2 h_2) & \sin(k_2 h_2) \\ e^{ikH}\sin(k_1 h_1) & e^{ikH}\cos(k_1 h_1) & \gamma\sin(k_2 h_2) & -\gamma\cos(k_2 h_2) \end{pmatrix} \begin{pmatrix} a_1 \\ b_1 \\ a_2 \\ b_2 \end{pmatrix} = \begin{pmatrix} 0 \\ 0 \\ 0 \\ 0 \end{pmatrix}. \quad (2.18)$$

The condition for the determinant to be zero leads to a non-trivial relation between the frequency ω and the effective wavenumber k :

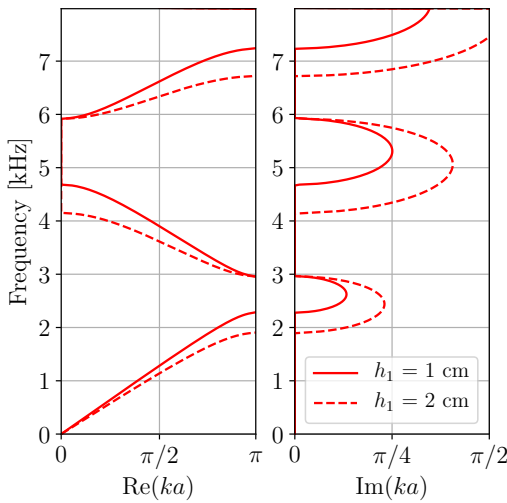
$$\cos(kH) = \cos(k_1 h_1)\cos(k_2 h_2) - \frac{1}{2} \left(\gamma + \frac{1}{\gamma} \right) \sin(k_1 h_1)\sin(k_2 h_2). \quad (2.19)$$

This relation is exact and allows to plot the real and complex part of the dispersion relation. The dispersion relation links the effective spatial wavenumber k to the temporal frequency ω . In free space, the dispersion relation is simply $k_0 = \frac{\omega}{c_0} = \frac{2\pi f}{c_0}$.

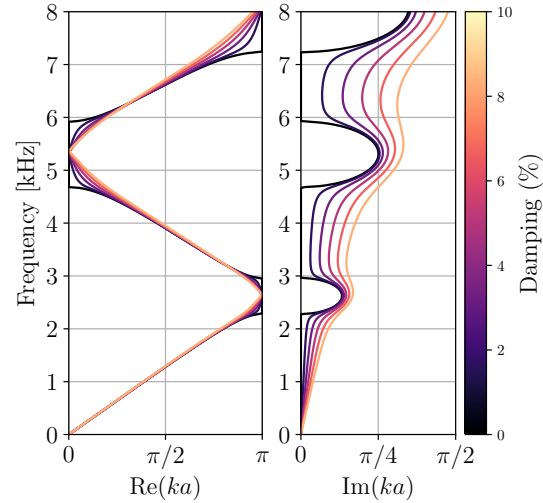
We consider an example configuration with steel plates embedded in water with the following parameters:

- 1 cm steel layer: $\rho_1 = 7800 \text{ kg/m}^3$, $c_1 = 5000 \text{ m/s}$.
- 25 cm water layer: $\rho_2 = 1000 \text{ kg/m}^3$, $c_2 = 1481 \text{ m/s}$, 0 to 10 % damping.

The damping is added as an imaginary part in the medium speed of sound. The real and imaginary part of the dispersion relation (2.19) are shown in figure (2.3) for the proposed configuration. The main result is the appearance of forbidden frequency bands in which the energy of the wave decays exponentially.



(a) Influence of the steel layer width.



(b) Influence of water damping.

Figure 2.3: Real and imaginary part of the dispersion relation in 1D for a steel-water unit cell.

2.2.2 Finite size medium

A more general approach to compute the dispersion relation is via the transfer matrix. It allows to take into account more complex unit cells and compute the acoustic properties of a finite size medium. A typical set up is shown in figure (2.4). The transfer matrix links the

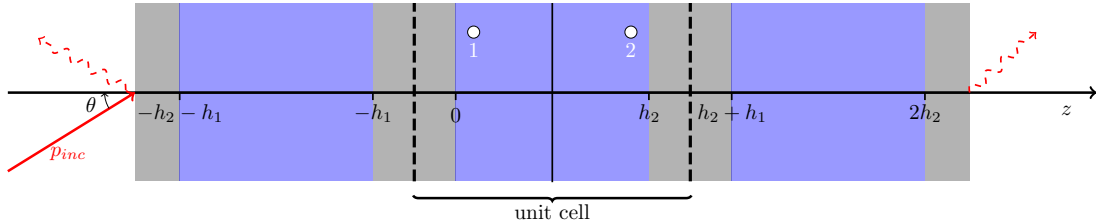


Figure 2.4: 1D symmetric finite size medium with 3 unit cells. The incident wave p_{inc} is transmitted and reflected by the medium.

acoustic pressure and velocity within a layer. For instance, the points 1 and 2 in figure (2.4) are related by:

$$\begin{pmatrix} p_1 \\ v_1 \end{pmatrix} = \begin{pmatrix} T_{11} & T_{12} \\ T_{21} & T_{22} \end{pmatrix} \begin{pmatrix} p_2 \\ v_2 \end{pmatrix}. \quad (2.20)$$

If θ is the angle of incidence of the incoming wave, the coefficients of the transfer matrix for the layer j are given by:

$$\mathbb{T}_j = \begin{pmatrix} T_{11} & T_{12} \\ T_{21} & T_{22} \end{pmatrix} = \begin{pmatrix} \cos(k_j h_j \cos \theta) & i \frac{Z_j \sin(k_j h_j \cos \theta)}{\cos \theta} \\ i \frac{\sin(k_j h_j \cos \theta)}{Z_j} \cos \theta & \cos(k_j h_j \cos \theta) \end{pmatrix}. \quad (2.21)$$

The transfer matrix can be multiplied to create multi-layer configurations:

$$\mathbb{T}_N = \prod_{j=1}^N \mathbb{T}_j. \quad (2.22)$$

If the transfer matrix is known, it can be shown that the dispersion relation for the effective wavenumber k is:

$$\cos(kH) = \frac{1}{2} (T_{11} + T_{22}). \quad (2.23)$$

This relation allows to define the dispersion relation for a more complex unit cell. We introduce the impedance of the host medium $Z_0 = \rho_0 c_0$. From the transfer matrix, the transmission coefficient can be obtained by:

$$\mathcal{T} = \frac{1}{4} \left(T_{11} + \frac{T_{12}}{Z_0} \cos \theta + \frac{T_{21} Z_0}{\cos \theta} + T_{22} \right)^2 \quad (2.24)$$

and the transmission loss in decibels is:

$$\text{TL} = 10 \log(\mathcal{T}). \quad (2.25)$$

Until now, a single incident plane wave has been considered to excite the medium. For a diffuse field excitation, the transmission loss can be obtained by integration over several incidence angles:

$$\tau = \frac{\int_0^{\theta_{\max}} \mathcal{T}(\theta) \cos(\theta) \sin(\theta) d\theta}{\int_0^{\theta_{\max}} \cos(\theta) \sin(\theta) d\theta}. \quad (2.26)$$

We consider the configuration shown in figure (2.4), namely the unit cell is a steel and water multi-layer. 3% damping is considered in the water layer. The transmission loss is computed under normal incidence ($\theta = 0$) and under a diffuse field for $\theta \in [0, \pi/2]$. The transmission loss and effective impedance for the finite and infinite media are compared. The effective impedance can be retrieved from the transfer matrix. The results are gathered in figure (2.5). The results show that the more unit cells, the closer to the infinite media behaviour. A

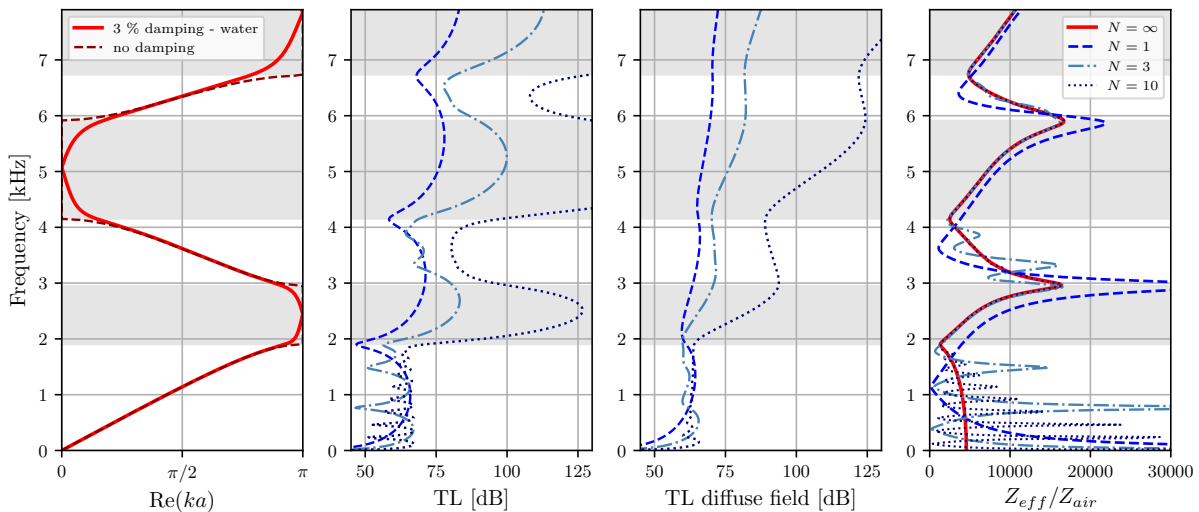


Figure 2.5: From left to right: dispersion relation of the infinite medium with and without damping, transmission loss through a finite number N of unit cells under normal incident plane wave, transmission loss through a finite number N of unit cells under diffuse field, effective impedance of the infinite and finite media. The grey areas correspond to the band gaps.

higher damping value increase the transmission loss, but reduce the effect of the band gap. At low frequencies, the finite size of the medium leads to Fabry-Perot resonances, which can be explained by the homogenization theory.

2.3 Two dimensional sonic crystal

There exists numerous numerical techniques to compute sonic crystals properties in higher dimensions [20, 21]. Without being exhaustive, we can cite the finite-difference time-domain (FDTD), multiple scattering theory (MST), finite element method (FEM), plane wave expansion (PWE) and homogenization theory. The problem to be solved can be of different nature depending of the crystal configuration: infinite, finite, waveguide or localized cavity. The main

parameters of influence are the geometry of the crystal, the type of periodicity, the host fluid and the filling fraction. In this part, 2D Helmholtz problems are solved with the finite element method. Three cases are analyzed:

1. An infinite sonic crystal,
2. A sonic crystal which is infinite in the y-axis but finite in the x-axis,
3. A finite sonic crystal in both the x-axis and y-axis.

From a physical point of view, the computation results elucidate acoustic transmission and diffraction properties.

2.3.1 Band structure of an infinite crystal

In this part, we consider a 2D unit cell made of acoustic rigid inclusions. We compute the dispersion relation in the associated periodic medium by finite element discretization. The obtained solution is compared with the plane wave expansion technique. A typical geometry of the problem is presented in figure (2.6). The starting point of the numerical computation

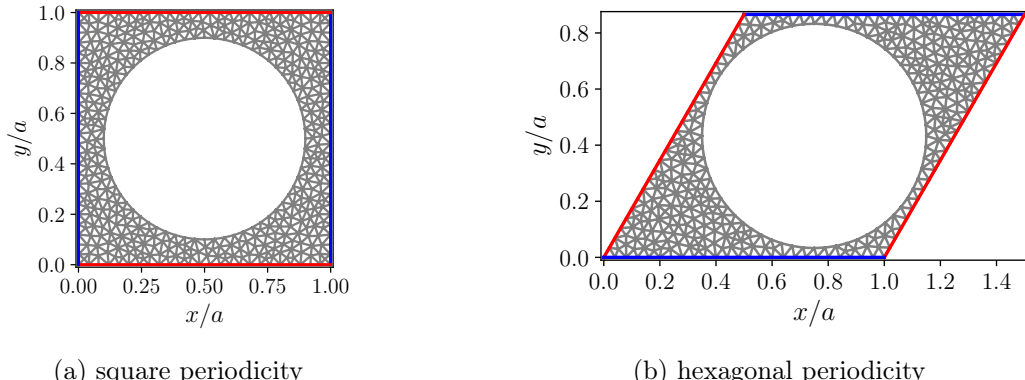


Figure 2.6: Mesh examples of the unit cell for finite element discretization. The colored lines illustrate the periodic boundary conditions.

is the Helmholtz equation without sources. We are looking for the pressure field p in a certain functional space V solution of:

$$\begin{aligned} \Delta p(\mathbf{x}) + \frac{\omega^2}{c_0^2} p(\mathbf{x}) &= 0, \quad \mathbf{x} \in \Omega, \\ \frac{\partial p}{\partial \mathbf{n}}(\mathbf{x}) &= 0, \quad \mathbf{x} \in \partial\Omega_{\text{int}}, \end{aligned} \tag{2.27}$$

where Ω is the mesh domain of the unit cell, \mathbf{n} the outward pointing normal and $\partial\Omega_{\text{int}}$ the boundary of the internal domain. A zero Neumann boundary condition is imposed because the sonic crystal is supposed acoustically rigid. Equation (2.27) needs to be solved with periodicity constraints. They are derived from Bloch theorem. For the square periodicity, it gives:

$$\begin{aligned} p(0, y) &= p(a_{1,x}, y) e^{i K_x a_{1,x}}, \quad y \in [0, a_{2,y}], \\ p(x, 0) &= p(x, a_{2,y}) e^{i K_y a_{2,y}}, \quad x \in [0, a_{1,x}]. \end{aligned}$$

The variational formulation for p is obtained by multiplying equation (2.27) with the complex conjugate of a function $q \in V$ and integrating over the domain Ω . The problem is to find $p \in V$ such as:

$$\forall q \in V, \quad \int_{\Omega} \Delta p q^* d\Omega + \frac{\omega^2}{c_0^2} \int_{\Omega} p q^* d\Omega = 0,$$

where $*$ denotes the complex conjugate. After the use of Green's formula [22], the formulation becomes:

Find p such as:

$$\forall q \in V, \quad - \int_{\Omega} \nabla p \nabla q^* d\Omega + \int_{\partial\Omega} \frac{\partial p}{\partial \mathbf{n}} q^* d\gamma + \frac{\omega^2}{c_0^2} \int_{\Omega} p q^* d\Omega = 0. \quad (2.28)$$

With the Bloch boundary conditions, the boundary term in the x-direction of the variational formulation becomes:

$$\begin{aligned} \int_{\partial\Omega} \frac{\partial p}{\partial \mathbf{n}} q^* d\gamma &= - \frac{\partial p}{\partial x}(0, y) q^*(0, y) + \frac{\partial p}{\partial x}(a_{1,x}, y) q^*(a_{1,x}, y) \\ &= q^*(a_{1,x}, y) \left(\frac{\partial p}{\partial x}(a_{1,x}, y) - \frac{\partial p}{\partial x}(0, y) e^{-iK_x a_{1,x}} \right) \\ &= 0. \end{aligned}$$

This holds if one imposes the natural boundary conditions in the x and y-directions :

$$\begin{aligned} \frac{\partial p}{\partial x}(0, y) &= \frac{\partial p}{\partial x}(a_{1,x}, y) e^{iK_x a_{1,x}}, \quad y \in [0, a_{2,y}], \\ \frac{\partial p}{\partial y}(x, 0) &= \frac{\partial p}{\partial y}(x, a_{2,y}) e^{iK_y a_{2,y}}, \quad x \in [0, a_{1,x}], \end{aligned}$$

such as the boundary integral vanishes. The functional space V of the solution p is then defined as:

$$V = \{u \in H^1(\Omega), u(\mathbf{s}) = u(\mathbf{s} + \mathbf{R}) e^{i\mathbf{K} \cdot \mathbf{R}}, \mathbf{s} \in \partial\Omega\}.$$

The variational formulation can now be discretized. However, the Bloch boundary conditions can be difficult to implement. We will take advantage of the Bloch theorem and use periodic boundary conditions instead of Bloch periodic boundary conditions. Bloch theorem claims that if the medium properties are periodic, the solution has the form:

$$p(\mathbf{x}) = \tilde{p}(\mathbf{x}) e^{i\mathbf{K} \cdot \mathbf{x}}, \quad \tilde{p}(\mathbf{x} + \mathbf{R}) = \tilde{p}(\mathbf{x}). \quad (2.29)$$

and the gradient writes:

$$\nabla p(\mathbf{x}) = (\nabla \tilde{p}(\mathbf{x}) + i\mathbf{K} \tilde{p}(\mathbf{x})) e^{i\mathbf{K} \cdot \mathbf{x}}. \quad (2.30)$$

If we replace (p, q) by (\tilde{p}, \tilde{q}) in formulation (2.28), one obtains:

Find $\tilde{p} \in \tilde{V}$ such that:

$$\begin{aligned} \forall \tilde{q} \in \tilde{V}, \quad & \int_{\Omega} \nabla \tilde{p} \nabla \tilde{q}^* d\Omega + i\mathbf{K} \int_{\Omega} \tilde{p} \nabla \tilde{q}^* d\Omega - i\mathbf{K} \int_{\Omega} \nabla \tilde{p} \tilde{q}^* d\Omega \\ & + \mathbf{K}^2 \int_{\Omega} \tilde{p} \tilde{q}^* d\Omega = \frac{\omega^2}{c_0^2} \int_{\Omega} \tilde{p} \tilde{q}^* d\Omega. \end{aligned} \quad (2.31)$$

The space \tilde{V} refers to:

$$\tilde{V} = \{u \in H^1(\Omega), u(\mathbf{s}) = u(\mathbf{s} + \mathbf{R}), \mathbf{s} \in \partial\Omega\}.$$

The boundary integral term for the (\tilde{p}, \tilde{q}) formulation vanishes if we impose the natural boundary conditions:

$$\begin{aligned}\frac{\partial \tilde{p}}{\partial x}(0, y) &= \frac{\partial \tilde{p}}{\partial x}(a_{1,x}, y), \\ \frac{\partial \tilde{p}}{\partial y}(x, 0) &= \frac{\partial \tilde{p}}{\partial y}(x, a_{2,y}).\end{aligned}$$

The same strategy is used for the hexagonal periodicity. This variational formulation is discretized on a finite dimensional space $\tilde{V}_h \subset \tilde{V}$. We choose the space of piecewise linear functions associated to a periodic mesh triangulation \mathcal{T}_h of the domain Ω . For a fixed Bloch wavenumber \mathbf{K} , the global linear system is formed by adding the contribution of elementary matrices over the triangulation. It leads to a general eigenvalue problem:

$$\mathbb{A}\tilde{p}_h = \omega^2 \mathbb{B}\tilde{p}_h, \quad \tilde{p}_h \in \tilde{V}_h, \quad (2.32)$$

where the matrices are decomposed on the basis functions $(e_i)_{1 \leq i \leq N_{nodes}}$:

$$\mathbb{A}_{ij} = \int_{\mathcal{T}_h} (\nabla e_i \cdot \nabla e_j + i\mathbf{K}e_i \cdot \nabla e_j - i\mathbf{K}\nabla e_i \cdot e_j + \mathbf{K}^2 e_i \cdot e_j) d\Omega \quad (2.33)$$

$$\mathbb{B}_{ij} = \frac{1}{c_0^2} \int_{\mathcal{T}_h} e_i \cdot e_j d\Omega. \quad (2.34)$$

The eigenvalues ω^2 are found and sorted for each Bloch wavevector \mathbf{K} . The eigenvectors correspond to pressure Bloch eigenmodes. The first eigenvalues of the linear system (2.32) leads to the following results:

- The dispersion relation or band gap structure, where the the Bloch wavevector varies in the Irreducible Brillouin Zone.
- The Bloch eigenmodes for a fixed Bloch wavevector.
- The iso-frequency countours, where the the Bloch wavevector varies in the first Brillouin zone.

These results are shown in figure (2.7). Physical information about the behaviour of acoustic waves in the sonic crystal can be inferred from these plots. For instance, the group velocity vector of the wave is perpendicular to the iso-frequency countours [23]. The group velocity approaches zero on the first branch of the dispersion relation at the points X and M . Above this branch, there is a frequency range in which the wave is not allowed to propagate through the medium. It is called a full band gap. If the wave propagation is forbidden in only one direction, we will refer to a partial band gap. Results for hexagonal periodicity are shown in figure (2.8). Both media differ in the location of the full and partial band gap openings but have similarities in the first mode of the iso-frequency countours.

To sum up, solving the linear system (2.32) leads to an approximation of the solution of Helmholtz equation in an infinite periodic media. The computation can be done for an

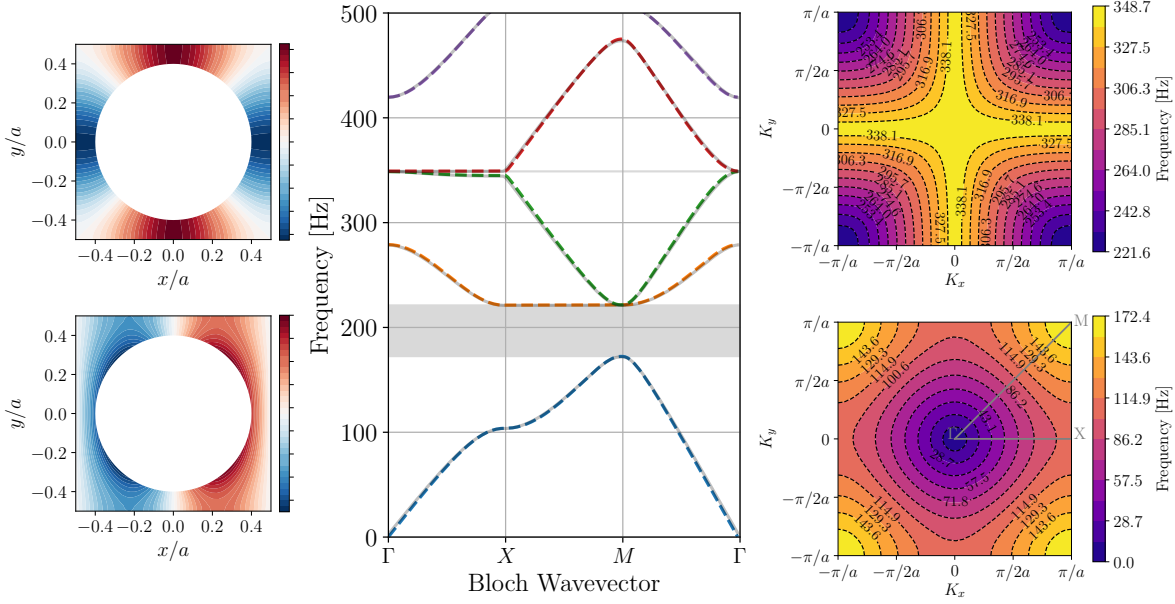


Figure 2.7: Physical properties of a sonic crystal with square periodicity and circle inclusions of radius $r = 0.4$. Left: Bloch eigenmode 0 (bottom) and 1 (top) for $(K_x, K_y) = (0, 0)$. Middle: Dispersion relation along the IBZ Γ -X-M of the periodic medium. Colored lines: FEM. Grey lines: Plane wave expansion. The grey bands enhance the band gaps. Right: Iso-frequency countours of the eigenmode 0 (bottom) and 2 (top).

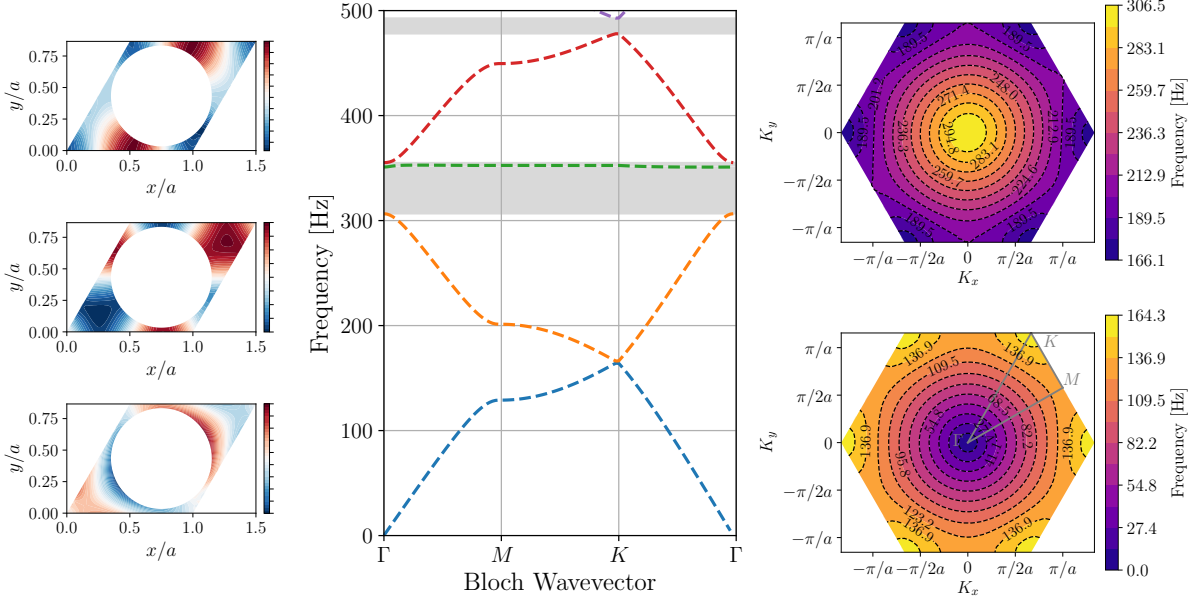


Figure 2.8: Physical properties of a sonic crystal with hexagonal periodicity and circle inclusions of radius $r = 0.4$. Left: Bloch eigenmode 0 (bottom), 1 (middle) and 2 (top) for $(K_x, K_y) = (0, 0)$. Middle: Dispersion relation along the IBZ Γ -M-K of the periodic medium. Colored lines: FEM. The grey bands enhance the band gaps. Right: Iso-frequency countours of the eigenmode 0 (bottom) and 1 (top).

arbitrary unit cell geometry. Note that since the finite element matrix in the system (2.32) is symmetric, only real eigenvalues can be computed. A further improvement would be to compute the imaginary part of the eigenvalues, which shows the strength of the band gap. This would require to break the symmetry of the problem and reformulate it in order to get a ω - \mathbf{K} formulation instead of the current \mathbf{K} - ω formulation [24, 25].

2.3.2 Transmission loss of a 1-direction finite sonic crystal

In this part, the Helmholtz transmission problem is solved for different geometries and numbers of unit cells. For the moment, the analysis is restricted to low frequencies. An example of the set up is shown in figure (2.9). The mesh domain is denoted by Ω and the external boundaries by $\Gamma = \bigcup_{i=1}^4 \Gamma_i$, where i is the subscript for respectively the left, bottom, right and top boundary. The internal boundaries are denoted by Γ_{int} . The normal of the boundaries \mathbf{n} is always outward pointing. Compared to the previous problem, one direction of the medium

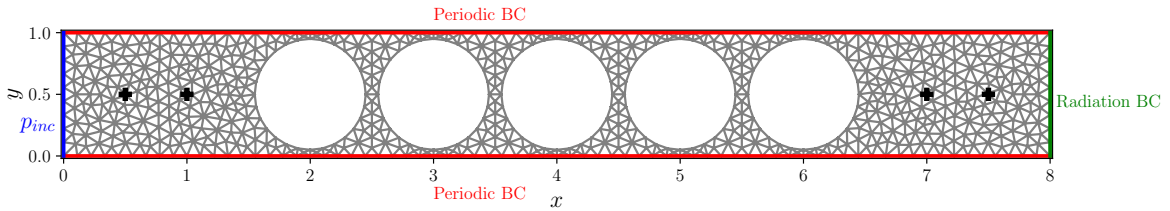


Figure 2.9: Mesh and set up of the one direction Helmholtz transmission problem.

is now of finite size. A plane wave is propagating in the x-direction. Periodic boundary conditions map the top to the bottom of the domain. The Helmholtz formulation writes:

$$\left. \begin{aligned} \Delta p(\mathbf{x}) + k_0^2 p(\mathbf{x}) &= 0, & \mathbf{x} \in \Omega, \\ \frac{\partial p}{\partial \mathbf{n}} &= p_{\text{inc}}, & \text{on } \Gamma_1, \\ \frac{\partial p}{\partial \mathbf{n}} &= p_{\text{out}}, & \text{on } \Gamma_3, \\ p(x, 1) &= p(x, 0), & \text{on } \Gamma_2 \cup \Gamma_4, \\ \frac{\partial p}{\partial \mathbf{n}}(x, 1) &= \frac{\partial p}{\partial \mathbf{n}}(x, 0), & \text{on } \Gamma_2 \cup \Gamma_4, \\ \frac{\partial p}{\partial \mathbf{n}} &= 0, & \text{on } \Gamma_{\text{int}}. \end{aligned} \right\} \quad (2.35)$$

For a normal incident plane wave along the x-direction, the input boundary condition is:

$$p_{\text{inc}} = ik_0. \quad (2.36)$$

And the output is a Robin boundary condition:

$$p_{\text{out}} = -ik_0 p. \quad (2.37)$$

This is a first order absorbing condition and the condition is exact as long as the plane wave assumption remains. We define the functional space for the variational formulation:

$$V = \{u \in H^1(\Omega), u(x, 1) = u(x, 0) \text{ on } \Gamma_2 \cup \Gamma_4\}.$$

The variational formulation of the transmission problem takes the form:

Find $p \in V$ such as:

$$\forall q \in V, \quad - \int_{\Omega} \nabla p \nabla q^* d\Omega + \int_{\Gamma} \frac{\partial p}{\partial \mathbf{n}} q^* d\gamma + k_0^2 \int_{\Omega} pq^* d\Omega = 0. \quad (2.38)$$

After the use of boundary conditions, the boundary term in the variational formulation becomes:

$$\int_{\Gamma} \frac{\partial p}{\partial \mathbf{n}} q^* d\gamma = - \int_{\Gamma_1} p_{inc} q^* d\gamma + ik_0 \int_{\Gamma_3} pq^* d\gamma, \quad (2.39)$$

where the integrals on Γ_2 and Γ_4 vanish because of the periodic boundary conditions. The formulation to be discretized is:

Find $p \in V$ such as:

$$\forall q \in V, \quad \int_{\Omega} \nabla p \nabla q^* d\Omega - ik_0 \int_{\Gamma_3} pq^* d\gamma - k_0^2 \int_{\Omega} pq^* d\Omega = \int_{\Gamma_1} ik_0 q^* d\gamma. \quad (2.40)$$

From there, an appropriate triangulation of the domain is built and the associated linear system assembled. The acoustic pressure p is computed on the mesh nodes for various wavenumbers k_0 .

We first validate the accuracy of the computation in an empty medium. We consider the exact solution $p_{ex}(x, y) = e^{ik_0 x}$. The error in the L2-norm is computed for two meshes with elements of size 0.1 and 0.05. Lagrange elements of order 1 and 2 are used. The L2 error over the mesh is defined as:

$$\text{Err}_{L_2(\Omega)} = \frac{\|p - \Pi p_{ex}\|_{L_2(\Omega)}}{\|\Pi p_{ex}\|_{L_2(\Omega)}}, \quad (2.41)$$

whre Πp_{ex} is the interpolation of the exact solution on the mesh nodes. Such Helmholtz problems are driven by the interpolation and dispersion error [26]. The interpolation error is due to the discretization of the solution and the dispersion error to the phase difference between the exact and approximate solution. Both error can be reduced by either refining the mesh or using high order elements. Figure (2.10) illustrates this behaviour by showing the error in the L2-norm for different mesh size and element order with an increasing number of elements per wavelength N . The running frequency is adapted with respect to N and the meshsize. Thereafter, quadratic elements with around twenty element per wavelength are used for the computations.

A finite size sonic crystal is added to the domain. We use the same unit cell as in the previous part, namely a circle of radius $r = 0.4$. Additional error might be introduced from the geometry discretization. The pressure is recorded at 4 locations inside the domain: 2 upstream and 2 downstream of the obstacle as shown in figure (2.9). The data are used to find the amplitude of the plane wave by plane wave decomposition. The transmission loss is computed in decibels by evaluating the ratio between the amplitudes of the incident and transmitted waves. Physically, the transmission loss represents the amount of sound pressure level attenuated by the sonic crystal.

Figure (2.11) presents the transmission loss at low frequencies for 1, 3 and 5 unit cells. The real part of the pressure is shown at the lower frequency of the second band gap, that

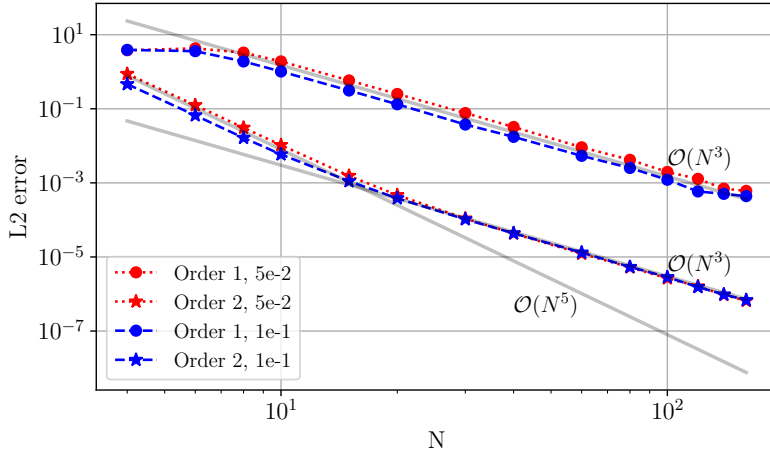


Figure 2.10: L2 Error assessment as a function of the number of elements per wavelength N for the Helmholtz 1-direction transmission problem in an empty medium for two mesh size with linear and quadratic elements. The running frequency is adjusted to the mesh size and N .

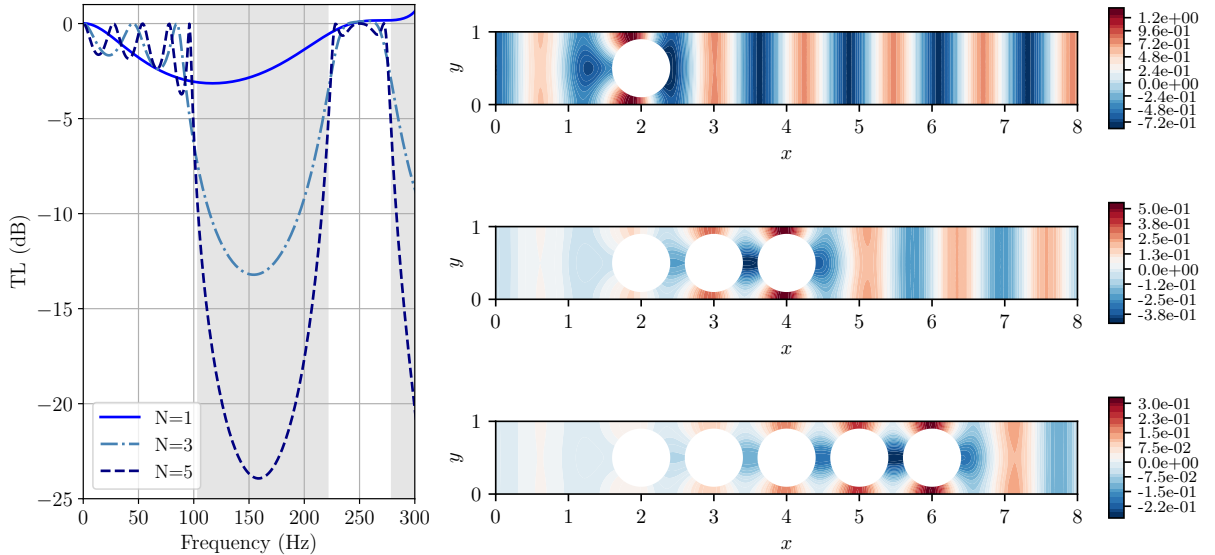


Figure 2.11: Left: transmission loss for a 1-direction finite sonic crystal composed of one, three and five layers. The grey area represents the band gap in the Γ -X direction. Right: Real part of the pressure field at 279 Hz. Note the analogy with the Bloch mode 1 in figure (2.7).

is 279 Hz. The more unit cells, the more the effect of the band gap becomes clear. At low frequencies, the finite size of the medium induces Fabry-Perot resonances.

From there, geometries can be combined in order to maximize the transmission loss [27]. For instance, an optimization algorithm could be implemented for that purpose [28].

2.3.3 Finite sonic crystal in 2-directions

We now study the case where the medium is finite in both the x and y-axis. Moreover, we would like to solve the Helmholtz problem for higher frequencies. An important issue from the discretization of this problem is the design of a proper radiation boundary condition.

We will use the Perfectly Matched Layer (PML) technique [29]. It consists in extending the computation domain by a layer of finite width in which the energy of the wave is decaying and non-reflecting. If designed correctly, this technique artificially recreates the Sommerfeld radiation condition. To implement the PML, the derivatives in the differential equation are modified by the transformation:

$$\frac{\partial}{\partial x} \mapsto \alpha(x) \frac{\partial}{\partial x}, \quad \alpha(x) = \frac{1}{1 + i \frac{\sigma(x)}{\omega}}, \quad (2.42)$$

for the x-direction. This modification is identical in the y-direction. The function σ is called the absorbing function. There are several choices for this function. We will use the Bermudez function [30, 31]. It is defined as:

$$\sigma(x) = \frac{\sigma}{\delta - (x - x_{\text{lim}}) + \epsilon}, \quad (2.43)$$

where $\sigma = c_0$ is the PML absorbing coefficient, δ is the width of the PML, x_{lim} is the limit of the physical domain and $\epsilon = 0.01$ is a small parameter for numerical stability. For the considered problem, the PML needs to be implemented in the x and y directions. The Helmholtz-PML formulation to be solved takes the form:

$$\begin{aligned} \alpha(x) \frac{\partial}{\partial x} \left(\alpha(x) \frac{\partial p}{\partial x} \right) + \alpha(y) \frac{\partial}{\partial y} \left(\alpha(y) \frac{\partial p}{\partial y} \right) + k_0^2 p &= 0, \quad \text{in } \Omega, \\ p &= 0, \quad \text{on } \Gamma_2 \cup \Gamma_3 \cup \Gamma_4, \\ \frac{\partial p}{\partial \mathbf{n}} &= p_{\text{inc}}, \quad \text{on } \Gamma_1, \\ \frac{\partial p}{\partial \mathbf{n}} &= 0, \quad \text{on } \Gamma_{\text{int}}. \end{aligned} \quad (2.44)$$

Figure (2.12) illustrates the numerical configuration. Dirichlet boundary conditions are used for the external domain. To derive the variational form of the above formulation, the Helmholtz-PML equation is first divided by the product $\alpha(x)\alpha(y) \neq 0$:

$$\frac{\partial}{\partial x} \left(\frac{\alpha(x)}{\alpha(y)} \frac{\partial p}{\partial x} \right) + \frac{\partial}{\partial y} \left(\frac{\alpha(y)}{\alpha(x)} \frac{\partial p}{\partial y} \right) + k_0^2 \frac{p}{\alpha(x)\alpha(y)} = 0. \quad (2.45)$$

The functional space for the variational formulation is set as:

$$V = \{u \in H^1(\Omega), u = 0 \text{ on } \Gamma_2 \cup \Gamma_3 \cup \Gamma_4\}.$$

The modified Helmholtz equation is multiplied by $q^* \in V$ and integrated over Ω . After the use of Green's formula, the variational formulation writes:

Find p in V such as:

$$\begin{aligned} \forall q \in V, \quad - \int_{\Omega} \frac{\alpha(x)}{\alpha(y)} \frac{\partial p}{\partial x} \frac{\partial q^*}{\partial x} d\Omega + \int_{\Gamma} \frac{\alpha(x)}{\alpha(y)} \frac{\partial p}{\partial x} q^* d\gamma - \int_{\Omega} \frac{\alpha(y)}{\alpha(x)} \frac{\partial p}{\partial y} \frac{\partial q^*}{\partial y} d\Omega \\ + \int_{\Gamma} \frac{\alpha(y)}{\alpha(x)} \frac{\partial p}{\partial y} q^* d\gamma + k_0^2 \int_{\Omega} \frac{pq^*}{\alpha(x)\alpha(y)} d\Omega &= 0. \end{aligned} \quad (2.46)$$

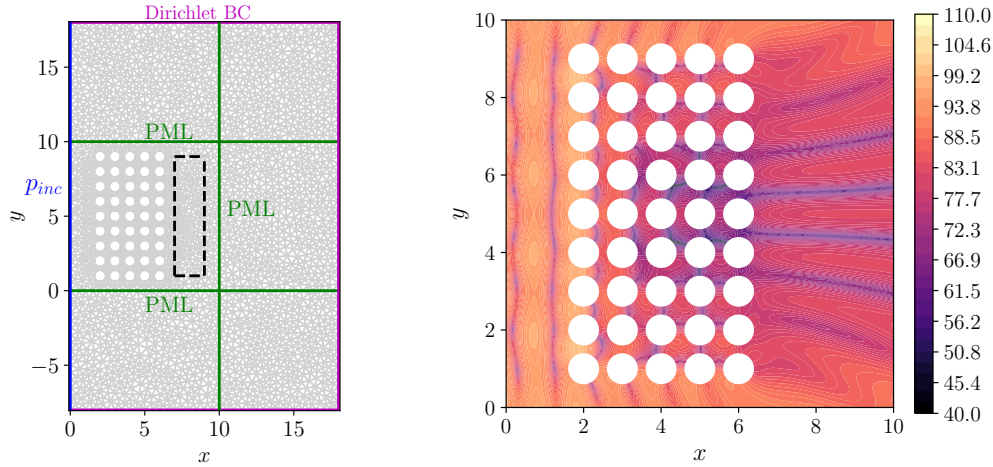


Figure 2.12: Left: typical set up for the 2D Helmholtz-PML problem with a 5×9 sonic crystal. Dashed black lines delimit the area for the measurement of the insertion loss. Right: pressure map in dB at 172 Hz.

The boundary conditions leads to:

Find p in V such as:

$$\forall q \in V, \quad \int_{\Omega} \left(\frac{\alpha(x)}{\alpha(y)} \frac{\partial p}{\partial x} \frac{\partial q^*}{\partial x} + \frac{\alpha(y)}{\alpha(x)} \frac{\partial p}{\partial y} \frac{\partial q^*}{\partial y} - k_0^2 \frac{pq^*}{\alpha(x)\alpha(y)} \right) d\Omega = \int_{\Gamma_1} p_{\text{inc}} q^* d\gamma. \quad (2.47)$$

This formulation is discretized on the mesh and the linear system assembled. To validate the computation, we use the parameters from table (2.1) in an empty medium. The incident

Frequency range [Hz]	FEM order	PML function	PML width	elem./ λ at 450 Hz
[50,450]	2	Bermudez, $\sigma = c_0$	$\delta = 8$	10

Table 2.1: Numerical parameters used to solve the Helmholtz-PML problem (2.44).

pressure p_{inc} is chosen to be a plane wave, such that the exact solution is $p_{\text{ex}} = e^{ik_0 x}$. The L2 error is recorded in the physical domain. For a given mesh, the L2 error decreases when the frequency increases, which shows that the error is mainly driven by the efficiency of the PML. At the lowest frequency (50 Hz) and for a PML width of $\delta = 8$, the maximal local error is of 6% and the global error reaches 35%. The error assessment is shown in figure (2.13). The empty case is then validated.

The next step is to run the computation for different types of sonic crystals. The influence of the number of layers in the y-direction is studied. For each frequency, the insertion loss is recorded. It is defined as:

$$\text{IL} = p_{\text{Empty case}}^{\text{dB}} - p_{\text{Sonic crystal}}^{\text{dB}}. \quad (2.48)$$

The insertion loss measures the sound pressure attenuation due to the sonic crystal. This quantity is averaged over a defined area in order to obtain a single value. The used area is delimited by the dashed black lines in figure (2.12).

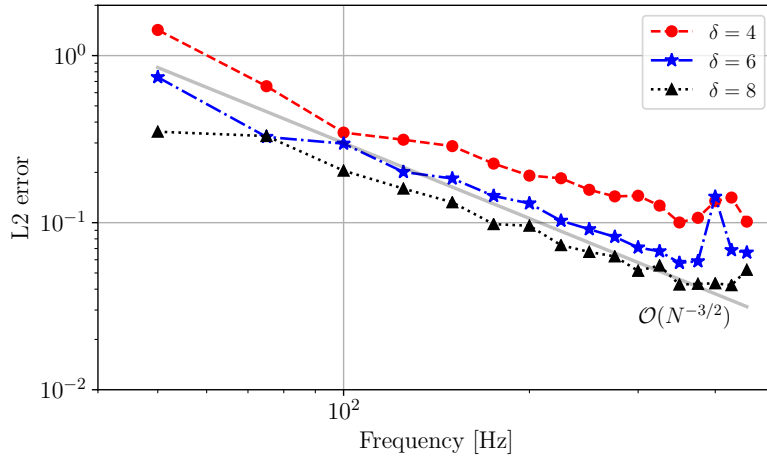


Figure 2.13: Error assessment of the Helmholtz-PML formulation in an empty medium for different PML width δ . The mesh is fixed and has 10 elements per wavelength at 450 Hz.

The integrated insertion loss is shown in figure (2.14) for a crystal with 5 unit cells in the x-direction and 1,5 and 9 unit cells in the y-direction. An example of the obtained pressure map in decibels is presented in figure (2.12). As the number of layers in the y-direction increase, the effect of periodicity becomes more significant. The insertion loss is higher inside the band gaps. The curves are more oscillating than in the 1D case because of the multiple scattering effects and the finite width of the crystal. The insertion loss is a quantity defined in the

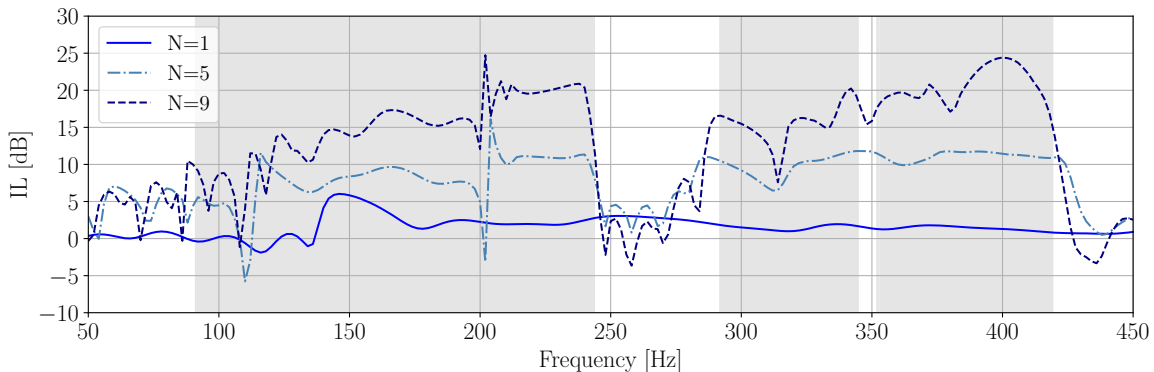


Figure 2.14: Integrated Insertion Loss of a 2D finite sonic crystal composed of 5×1 , 5×5 and 5×9 unit cells of radius $r = 0.45$. The grey areas represent the band gaps in the Γ -X direction.

entire space, and its interpretation as a single value might not be representative of the crystal behaviour. The sonic crystal seems to be efficient from four to five layers: an attenuation of at least 10dB is recorded in the near field in 2D.

Until now, the sonic crystal has been assumed invariant in the z-direction. The next part will investigate the 3D effect of sonic crystals.

Chapter 3

Preliminary development on the Launch Pad

In this chapter, the acoustic properties of a sonic crystal are demonstrated on a three dimensional engineering case. The goal is to simulate the exterior acoustic scattering during the launch of Vega. The noise reduction efficiency of a sonic crystal at the launch pad is investigated. The computations are based on boundary element formulations (BEM).

We start by explaining the used formulations and the high performance computing techniques. We assess the methodology on a simple case, the scattering of a sound-hard sphere. Then, the multiple scattering of a single sonic crystal is computed. Finally, we consider the scattering of the Vega launch Pad with and without the sonic crystal. The physical model of the problem is discussed. Two software were used to run the BEM computations: the commercial software VAOne [32, 33] and the open-source library Bempp [34, 35].

3.1 Boundary Element formulations

The three dimensional Helmholtz problem is approached by the boundary element method. Compared to the finite element method, it involves less unknowns in the linear system since only the geometry of the boundary has to be meshed. Furthermore, the Sommerfeld radiation condition is automatically satisfied. However, the matrix to be inverted is fully populated and might be ill-conditioned. The explanations of this section are inspired from [36].

3.1.1 Helmholtz problem and representation formula

We are looking for a solution p^{tot} of the Helmholtz equation in 3D, namely the total pressure field:

$$\Delta p^{\text{tot}} + \frac{\omega^2}{c_0^2} p^{\text{tot}} = 0, \quad \text{in } \Omega^+, \quad (3.1)$$

where p^{tot} is the sum of the incident and the scattered field: $p^{\text{tot}} = p^{\text{inc}} + p^{\text{sca}}$. The exterior domain Ω^+ is delimited by a smooth obstacle Γ and is unbounded. We define the domain $\Omega = \Omega^- \cup \Omega^+$ as the union of the interior and exterior domains. For hard-sound obstacles, the Helmholtz equation must satisfy the boundary conditions:

$$\begin{aligned} \frac{\partial p^{\text{tot}}}{\partial \mathbf{n}} &= 0 \quad \text{on } \Gamma, \\ \lim_{r \rightarrow +\infty} r \left(\frac{\partial p^{\text{sca}}}{\partial r} - ik_0 p^{\text{sca}} \right) &= 0, \end{aligned} \quad (3.2)$$

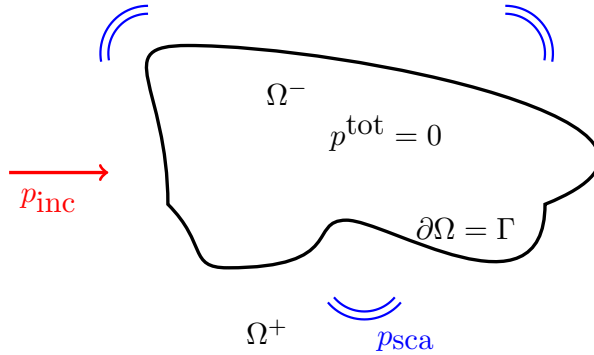


Figure 3.1: Sketch of the set up for the BEM formulation. The black line is the scatterer boundary $\partial\Omega = \Gamma$.

where $r = |\mathbf{x} - \mathbf{y}|$ is the distance between two points in the exterior domain. If we suppose $p^{\text{tot}} \in H_{\text{loc}}^1(\overline{\Omega^+})$, the Helmholtz problem has an unique solution [37]. The situation is resumed in figure (3.1). The obstacle is assumed to be impenetrable, so that the total field is zero in the interior domain: $p^{\text{tot}} = 0$ in Ω^- . A simple approach for the BEM is to write a weak form of the Helmholtz equation and transform the volume integral into a surface integral. The following lines explain a simple derivation of a so-called representation formula. We consider a solution of the Helmholtz equation $u \in H^1(\Omega)$. The first step is to multiply the Helmholtz equation by a test function $v \in H^1(\Omega)$ and integrate it over the domain $\Omega = \Omega^- \cup \Omega^+$:

$$\forall v \in H^1(\Omega), \quad \int_{\Omega} \Delta u v \, d\Omega + k_0^2 \int_{\Omega} u v \, d\Omega = 0. \quad (3.3)$$

We can apply Green's formula [22]:

$$\forall v \in H^1(\Omega), \quad - \int_{\Omega} \nabla u \nabla v \, d\Omega + \int_{\Gamma} \frac{\partial u}{\partial \mathbf{n}} v \, d\Gamma + k_0^2 \int_{\Omega} u v \, d\Omega = 0. \quad (3.4)$$

We apply Green's formula once more:

$$\forall v \in H^1(\Omega), \quad \int_{\Omega} u (\Delta v + k_0^2 v) \, d\Omega = \int_{\Gamma} \left(u \frac{\partial v}{\partial \mathbf{n}} - v \frac{\partial u}{\partial \mathbf{n}} \right) \, d\Gamma. \quad (3.5)$$

In linear acoustics, the Green function or free field impulse response in 3D is given by:

$$G(\mathbf{x}, \mathbf{y}) = \frac{e^{ik_0 r}}{r}, \quad r = |\mathbf{x} - \mathbf{y}|, \quad r \neq 0. \quad (3.6)$$

This function is the fundamental solution of the Helmholtz operator in 3D. The left term in equation (3.5) can be simplified if $\mathbf{x}, \mathbf{y} \in \Omega^+$:

$$\int_{\Omega} u(\mathbf{y}) (\Delta G(\mathbf{x}, \mathbf{y}) + k_0^2 G(\mathbf{x}, \mathbf{y})) \, d\Omega(\mathbf{y}) = \int_{\Omega} -u(\mathbf{y}) \delta(\mathbf{x}, \mathbf{y}) \, d\Omega(\mathbf{y}) = -u(\mathbf{x}), \quad (3.7)$$

δ being the Dirac delta function. The initial variational formulation becomes:

$$u(\mathbf{x}) = \int_{\Gamma} G(\mathbf{x}, \mathbf{y}) \frac{\partial u}{\partial \mathbf{n}}(\mathbf{y}) - u(\mathbf{y}) \frac{\partial G}{\partial \mathbf{n}}(\mathbf{x}, \mathbf{y}) \, d\Gamma(\mathbf{y}), \quad \mathbf{x} \in \Omega^+, \mathbf{y} \in \Gamma. \quad (3.8)$$

This is a representation formula for any $\mathbf{x} \in \Omega^+$ and for any radiating solution u of the Helmholtz equation. It is also known as Kirchhoff–Helmholtz integral. It allows to evaluate the pressure field in the exterior domain if the pressure is known on the boundary. We can now define the single and double potential operators, which are respectively:

$$\mathcal{V}\psi(\mathbf{x}) = \int_{\Gamma} G(\mathbf{x}, \mathbf{y})\psi(\mathbf{y})d\Gamma(\mathbf{y}), \quad \mathbf{x} \in \Omega \setminus \Gamma \quad (3.9)$$

$$\mathcal{K}\phi(\mathbf{x}) = \int_{\Gamma} \frac{\partial}{\partial \mathbf{n}(\mathbf{y})} G(\mathbf{x}, \mathbf{y})\phi(\mathbf{y})d\Gamma(\mathbf{y}), \quad \mathbf{x} \in \Omega \setminus \Gamma. \quad (3.10)$$

The representation formula in the exterior domain becomes:

$$u(\mathbf{x}) = (\mathcal{V}\psi)(\mathbf{x}) - (\mathcal{K}\phi)(\mathbf{x}), \quad \mathbf{x} \in \Omega^+ \setminus \Gamma, \quad (3.11)$$

where $\psi = \frac{\partial u}{\partial \mathbf{n}}$ and $\phi = u$ are the surface potentials who are defined on the boundary. With a Neumann boundary condition, the potential $\psi = \frac{\partial u}{\partial \mathbf{n}}$ is zero and the representation formula only needs to evaluate the double potential operator \mathcal{K} . To compute the surface potentials on the boundary Γ , appropriate mathematical tools need to be considered.

3.1.2 Trace operators and Boundary Integral Equations

The trace operators map a function from a domain onto the boundary, provided that the boundary is sufficiently smooth, or more precisely Lipschitz continuous. We will use two trace operators: the Dirichlet trace γ_0 and Neumann trace γ_1 . The Dirichlet trace γ_0 might be defined as:

$$\gamma_0 : \begin{cases} H^1(\Omega) \rightarrow L^2(\partial\Omega) \\ u \mapsto \gamma_0(u) := u|_{\Gamma} \end{cases},$$

and we define the fractional Sobolev space:

$$H^{1/2}(\Gamma) = \{u \in L^2(\partial\Omega); \exists \tilde{u} \in H^1(\Omega), u = \gamma_0(\tilde{u})\}.$$

The fractional Sobolev space contains functions living on the boundary. Roughly speaking, if a function $u \in H^1(\Omega)$ is projected on the boundary, it loses a half-derivative. With the above definition, the trace operator γ_0 is a continuous linear operator in the sense that γ_0 is bounded by the $H^1(\Omega)$ norm. The Neumann trace γ_1 is usually defined in $H^2(\Omega)$. However, It can be also be defined in $H^1(\Delta, \Omega)$:

$$\gamma_1 : \begin{cases} H^1(\Delta, \Omega) \rightarrow L^2(\partial\Omega) \\ u \mapsto \gamma_1(u) := \frac{\partial u}{\partial \mathbf{n}}|_{\Gamma} \end{cases},$$

and the associated fractional Sobolev space:

$$H^{-1/2}(\Gamma) = \{u \in L^2(\partial\Omega); \exists \tilde{u} \in H^1(\Delta, \Omega), u = \gamma_1(\tilde{u})\}.$$

These two Sobolev spaces form the dual pair $\langle \cdot, \cdot \rangle_{H^{-1/2}, H^{1/2}}$. It can be shown that the trace operator γ_1 is bounded by the $H^1(\Delta, \Omega)$ norm [38]. These trace operators can be defined either in the internal or external domain. They are denoted respectively by γ^- and γ^+ .

From these definitions, the representation formula for the scattered field p^{sca} takes the form:

$$p^{\text{sca}} = \mathcal{V}(\gamma_1^- p^{\text{sca}} - \gamma_1^+ p^{\text{sca}}) - \mathcal{K}(\gamma_0^- p^{\text{sca}} - \gamma_0^+ p^{\text{sca}}), \quad (3.12)$$

which can be simplified to:

$$p^{\text{sca}} = \mathcal{K}(\gamma_0^+ p^{\text{tot}}). \quad (3.13)$$

We now define the boundary integral operators:

$$K\phi(\mathbf{x}) = \int_{\Gamma} \frac{\partial G}{\partial \mathbf{n}(\mathbf{y})}(\mathbf{x}, \mathbf{y})\phi(\mathbf{y})d\Gamma(\mathbf{y}), \quad \mathbf{x} \in \Gamma, \quad (3.14)$$

$$D\phi(\mathbf{x}) = -\frac{\partial}{\partial \mathbf{n}(\mathbf{x})} \int_{\Gamma} \frac{\partial G}{\partial \mathbf{n}(\mathbf{y})}(\mathbf{x}, \mathbf{y})\phi(\mathbf{y})d\Gamma(\mathbf{y}), \quad \mathbf{x} \in \Gamma, \quad (3.15)$$

where $K : H^{1/2}(\Gamma) \mapsto H^{1/2}(\Gamma)$ is the double-layer boundary integral operator and $D : H^{1/2}(\Gamma) \mapsto H^{-1/2}(\Gamma)$ the hypersingular boundary integral operator. The jump relations across Γ are given by:

$$K\phi = \gamma_0^-(\mathcal{K}\phi) + \frac{1}{2}\phi = \gamma_0^+(\mathcal{K}\phi) - \frac{1}{2}\phi, \quad (3.16)$$

$$D\phi = -\gamma_1^-(\mathcal{K}\phi) = -\gamma_1^+(\mathcal{K}\phi). \quad (3.17)$$

We can now apply the trace operators on the representation formula (3.13). The interior Dirichlet trace gives:

$$-\gamma_0^+ p^{\text{inc}} = K(\gamma_0^+ p^{\text{tot}}) - \frac{1}{2}(\gamma_0^+ p^{\text{tot}}), \quad (3.18)$$

and the exterior Neumann trace γ_1^+ gives:

$$-\gamma_1^+ p^{\text{inc}} = -D(\gamma_0^+ p^{\text{tot}}). \quad (3.19)$$

It is now possible to determine p^{tot} on Γ with either (3.18) or (3.19). However, the above boundary integral equations are known to be singular. We define a coupling parameter $\eta \in \mathbb{C}$. A linear combination of (3.18) and (3.19) leads to the Burton-Miller formulation:

$$\left(\frac{1}{2}I - K\right)p^{\text{tot}} + \eta Dp^{\text{tot}} = p^{\text{inc}} + \eta \partial_n p^{\text{inc}} \quad \text{on } \Gamma. \quad (3.20)$$

This equation has an unique solution $p^{\text{tot}} \in H^{1/2}(\Gamma)$ if $\text{Im}(\eta) \neq 0$. In VAOne, this boundary equation is used with the empirical value $\eta = 0.03 \frac{i}{k_0}$ [32].

However, one might notice that the operator $(\frac{1}{2}I - K)$ maps from $H^{1/2}(\Gamma)$ to $H^{1/2}(\Gamma)$ whereas the hyper-singular operator maps from $H^{1/2}(\Gamma)$ to $H^{-1/2}(\Gamma)$. This difference in the functional spaces can explain that the Burton-Miller formulation faces convergence issues at high frequencies. In Bempp, the hyper-singular operator is regularized such that all operators are well defined on $H^{1/2}(\Gamma)$. The regularization is based on a local surface approximation of the exterior Neumann-to-Dirichlet map. The approximation is defined as:

$$N^{\text{osrc}} = \frac{1}{ik_0} \left(1 + \frac{\Delta_{\Gamma}}{k_{\epsilon}^2}\right), \quad k_{\epsilon} = k_0(1 + i\epsilon), \quad \epsilon = 0.4(k_0 R)^{-2/3}, \quad (3.21)$$

where Δ_Γ is the Laplace-Beltrami operator and R the radius of the obstacle. The localization of the operator is done with a Padé approximation of small size. This helps to achieve the regularization in a reasonable time. The regularized formulation or On-Surface Radiation Condition (OSRC) preconditioned Burton-Miller formulation writes:

$$\left(\frac{1}{2}I - K\right)p^{\text{tot}} + N^{\text{osrc}}Dp^{\text{tot}} = p^{\text{inc}} + N^{\text{osrc}}\partial_n p^{\text{inc}} \quad \text{on } \Gamma. \quad (3.22)$$

This formulation has an unique solution in $H^{1/2}(\Gamma)$ if $\epsilon \neq 0$. For any wavenumber k_0 and on a smooth surface Γ , both Burton-Miller and OSRC-preconditioned Burton-Miller formulations admit an unique solution.

3.2 Discretization, system preconditioning and fast algorithms

Two techniques are mainly used to discretize BEM formulations: The Galerkin and the collocation methods. The collocation method simply applies the operators on a set of suitable points, for instance the mesh nodes. It requires that the boundary equation is satisfied for all these points. It involves only one integral to solve but the resulting matrix is not symmetric. From a practical point of view, this method has shown its efficiency. However, there is few or no convergence result that proves the stability of this procedure.

The Galerkin method writes the BEM formulation in a variational form. The resulting operators are symmetric and the assembly can be done on non-smooth domains. Convergence results have been established. The Galerkin method is more difficult to set up than the collocation method since it involves for instance the evaluation of double integrals.

The matrices resulting from the boundary integrals discretization are fully-populated and might be large. With a pure BEM approach, the memory requirements grow with a complexity of $\mathcal{O}(N^2)$, where N is the number of degrees of freedom. This would only be possible for small problems. Acceleration techniques have been developed to reduce the memory requirements and speed up the resolution of the BEM linear system. The idea is to accelerate the matrix-vector product for the iterative solver without explicitly assemble the BEM matrix. In VAOne, the Fast Multipole Method (FMM) is implemented while the Hierarchical matrix or \mathcal{H} -matrix compression is implemented in Bempp. The basic idea of the FMM and \mathcal{H} -matrix compression is to split the BEM matrix into a near field and far field part. If the current pressure field approximation of the iterative solver is denoted by p_k and the BEM matrix by A , the matrix-vector product for the iterative solver is [39]:

$$Ap_k = (A_{\text{near}} + A_{\text{far}})p_k = A_{\text{near}}p_k + y_{\text{far}}.$$

The matrix A_{near} is banded and sparse and is evaluated as in the classic BEM. The FMM and \mathcal{H} -matrix methods differ in the evaluation of y_{far} . Both methods divides the degrees of freedom into a cluster tree.

- In the VAOne FMM, y_{far} is approximated by an expansion of the Helmholtz kernel in spherical harmonics, which separates the spatial variables. The quality of the approximation depends on the frequency and the distance between the points. An illustrative explaination of the FMM can be found in [40].

- In the Bempp \mathcal{H} -matrix, the matrix A_{far} is compressed by a low rank approximation, which is obtained by an Adaptative Cross Approximation (ACA) algorithm. It allows a quick evaluation of y_{far} . Usually, the \mathcal{H} -matrix method uses more memory for the set up compared to the FMM, but has faster matrix-vector product [41].

Both method are supposed to reduce the time and memory requirements complexities to $\mathcal{O}(N \log N)$ or more. These acceleration techniques are purely algorithm improvements and are of great interest in various physical areas such as electromagnetic, seismic or medical.

Finally, Bempp uses the GMRES iterative solver while VAOne uses the fGMRES solver with a variant of an Incomplete LU preconditioner, called ILUT. Note that Bempp automatically applies the inverse of the mass matrix to the compressed BEM matrix by computing its LU factorization. Table (3.1) resumes the main features of the two solvers.

	Formulation	Discretization	Acceleration	Linear solver
Bempp	Burton-Miller with operator preconditioning	Galerkin	H-matrix	GMRES
VAOne	Burton-Miller	Collocation	FMM	ILUT+fGMRES

Table 3.1: VAOne and bempp main features comparison.

To sum up, the resolution of the Helmholtz equation is done in two steps:

1. Solve the linear system for the unknowns living on the boundary of the domain.
2. Use the representation formula to compute the pressure field at any point in space.

Both step can be accelerated by the FMM or the \mathcal{H} -matrix compression.

3.3 Scattering of a sound-hard sphere

We investigate the accuracy of the solver by the classical example of the sound-hard sphere scattering. A plane wave $p^{\text{inc}} = e^{ik_0 x}$ impinges a sphere of radius $R = 1$ following the positive x-axis. The pressure response of the total field is recorded around a circle of radius $r = 3$. The frequency range is set to $[100, 700]$ Hz. The mesh size is set such as there is 10 elements per wavelength. For example, the meshes for 100 and 700 Hz contain respectively 179 and 6682 degrees of freedom. For a polar point (r, θ) in the 2D plane, the analytic solution of the problem is [42]:

$$p^{\text{sca}}(r, \theta) = \sum_{n=1}^{\infty} c_n (j_n(k_0 r) - i n_n(k_0 r)) P_n(\cos \theta), \quad (3.23)$$

$$c_n = -(2n+1)(-i)^n \frac{j'_n(k_0 R)}{2j'_n(k_0 R) - h'_n(k_0 R)}, \quad (3.24)$$

where P_n is the Legendre polynomial of order n , j_n and n_n are respectively the spherical Bessel functions of the 1st and 2nd kind and h_n denotes the Spherical Hankel function of the 1st kind. The prime ' denotes the derivative of these special functions.

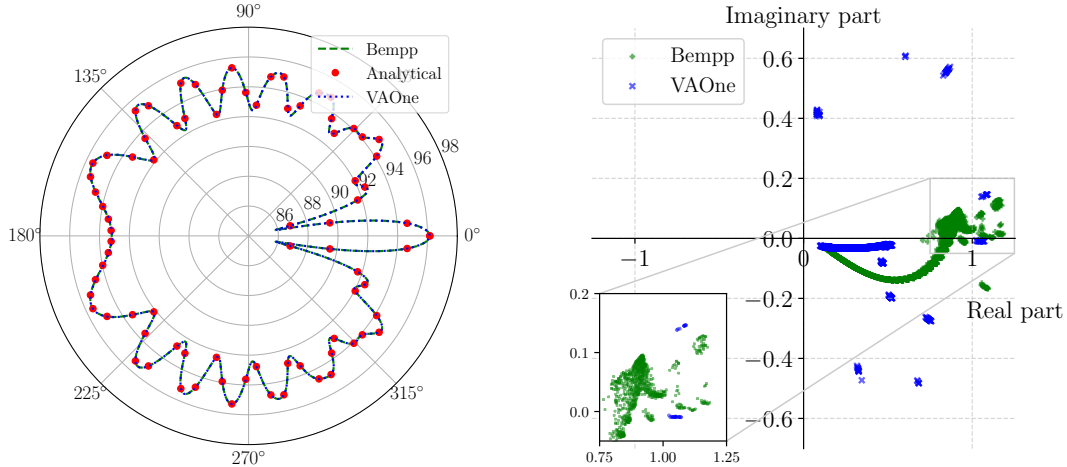


Figure 3.2: Left: total directivity pressure response of a sound-hard sphere by a plane wave. Right: corresponding normalized eigenvalues of the BEM matrix for the two formulations.

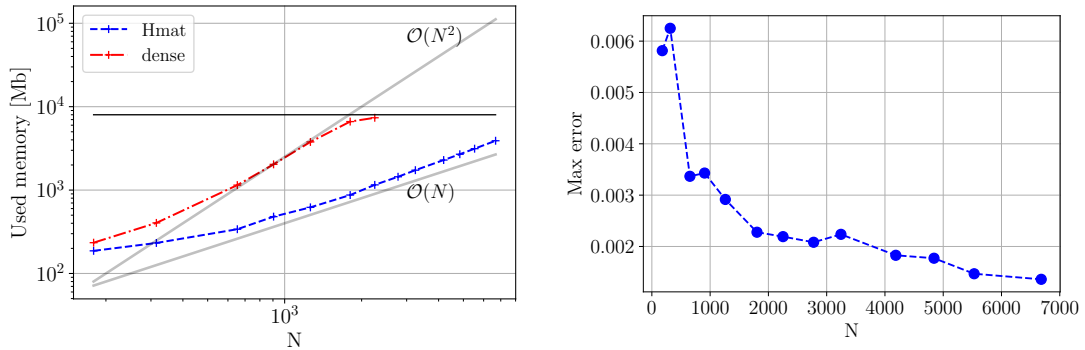


Figure 3.3: Left: used memory for the Bempp solver in the \mathcal{H} -matrix mode and in the classical dense mode. The black line shows the available RAM on the machine. Right: maximal error of the polar data as a function of the number of dofs. The excitation frequency is adapted to keep 10 elements per wavelength.

Figure (3.2) shows the total acoustic pressure for $kR = 10$. The eigenvalues for the Burton-Miller and Regularized Burton-Miller formulation are shown for this same frequency. For a tolerance of $1e-5$ in the GMRES solver, the Burton-Miller formulation has been solved in 14 iterations and the regularized Burton-Miller in 5 iterations. This is a direct consequence of the eigenvalues distribution.

The memory consumption of Bempp for the \mathcal{H} -matrix and dense mode is shown in figure (3.3). In terms of resolution time, we observe as well a complexity of approximately $\mathcal{O}(N^2)$ for the dense mode and $\mathcal{O}(N)$ for the \mathcal{H} -matrix mode. The error in maximum norm of the polar plot is reported. The error is decreasing with the number of dofs because the mesh capability to represent the sphere becomes better.

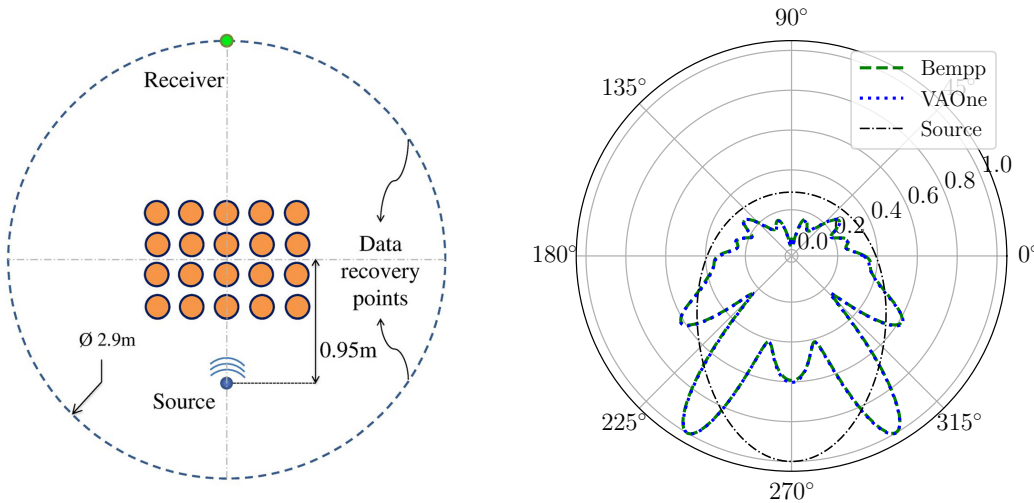
3.4 Scattering of a cylindrical array of scatterers

This case allows to validate the Bempp and VAOne solvers on a more realistic case and understand the effect of a 3D sonic crystal. The set up is taken from the work of Kamiri [43], where it was used to validate periodic BEM solvers. Two sonic crystal are considered: one with cylindrical unit cell and one with an inner resonator. The same set up is used:

1. A spherical source, here an acoustic monopole, impinges a 4×5 sonic crystal.
2. the pressure is recorded on a grid in the X-Y plane and on a polar plot.

The situation is resumed in figure (3.4a). The sonic crystal is meshed with around 10 elements per wavelength. Around 20 elements are used around the cylinders to reduce geometric discretization errors. The frequency range is set from 100 to 1000 Hz.

The polar plot in figure (3.4b) compares the total pressure field obtained with both solvers at 687.5 Hz in the $z = 0$ plane. The methods are in good agreement with the polar plot from the study of Karimi [43]. We can gather the polar plots and analyze the reflected angles over



(a) Simulation set up for the scattering of a 4×5 sonic crystal, extracted from [43]. (b) Normalized polar pressure response for the total field at 687.5 Hz.

Figure 3.4: Set up and directivity result of the acoustic scattering by a sonic crystal.

frequencies. A 2 Hz step is used. The polar pressure response is recorded for each frequency. With the tools developed in the previous chapter, it is interesting to compare the obtained results with the band gap structure of the sonic crystal in the Γ - X direction. The results are resumed in figure (3.5) and illustrate the different working regimes of the sonic crystals.

Compared to the single sphere case, the multiple scattering effect of the sonic crystal increase the conditioning of the BEM matrix. This effect is amplified with the presence of inner resonators. In VAOne, the ILUT preconditioning helps to speed up the convergence of the iterative solver compared to Bempp, where only the mass matrix of the system is applied for preconditioning. For a fixed GMRES accuracy, the number of iterations needed to solve the system is in average two to three times more in Bempp than in VAOne. For this case, the

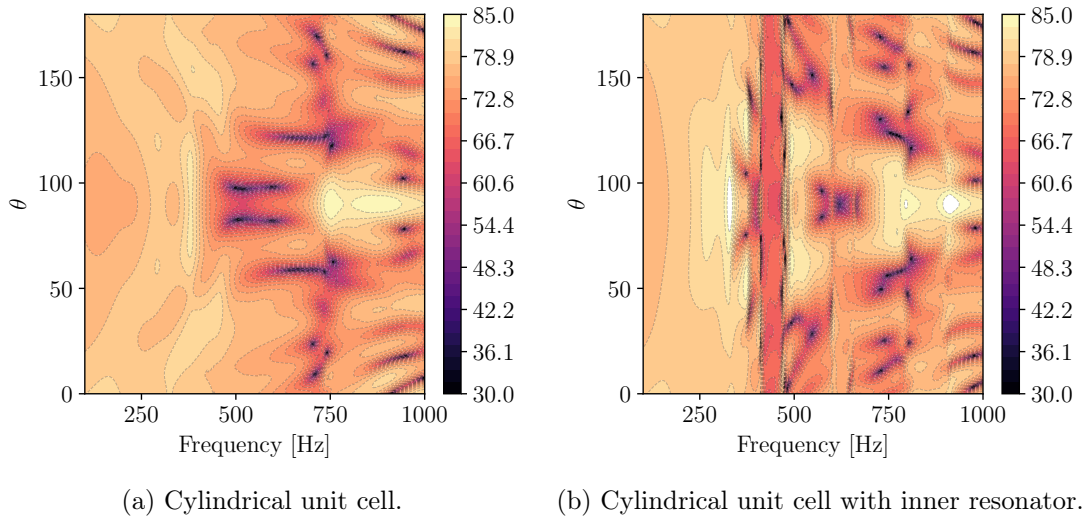


Figure 3.5: Directivity of the total pressure response in dB downstream of two different sonic crystals in the frequency range [100, 1000] Hz. The monopole source is set to 1 Pa.

method with system preconditioning seems more suitable than with operator preconditioning.

3.5 Scattering of the Vega launch pad

In this section, we study a full scale engineering case: the sound radiation from the Vega launch pad. A mimic of the launch pad geometry has been created. The associated mesh is shown in figure (1.4). The depicted mesh has around 87k nodes. We are interested in the

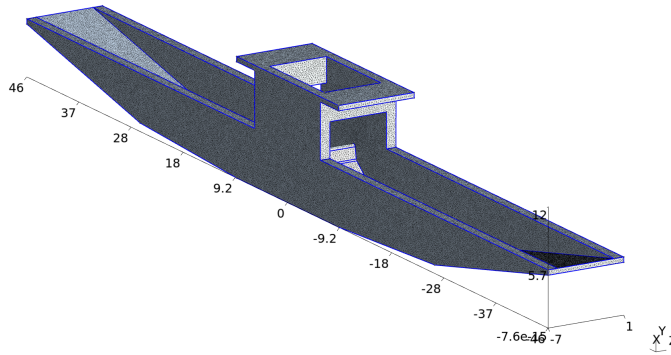


Figure 3.6: Example of a triangulation from the Vega launch pad. The coordinates are in meters.

sound radiated by the Vega launch vehicle. We suppose that the main source of noise comes from the exhaust plume, which is modeled by a single acoustic monopole. The amplitude of the source is normalized to 1 Pa. We are interested in the far field response of the launch pad, especially at the location of the rocket fairing, where the radiated sound has a direct impact

on the payload. Two configurations are considered:

- The ignition phase, where the monopole is placed close to the launch pad. The source location is $(x_s, y_s, z_s) = (0, 11, -3)$.
- The lift-off phase, where the monopole is placed above the launch pad. The source location is $(x_s, y_s, z_s) = (0, 30, -3)$.

According to the specifications from figure (1.2), the maximum sound pressure level is reached in the frequency band from 250 to 500 Hz. The size of the launch pad is around 100 meters, which gives an adimensional wavenumber ka of at least 500 for 250 Hz. The resolution of the Helmholtz equation of such a problem with the BEM technique comes with important issues:

- The oscillatory behaviour of Helmholtz Kernel. For instance, the FMM solver in VAOne is limited to 160 Hz for this case.
- The large number of degrees of freedom. For instance, a simulation at 500 Hz with 10 elements per wavelength would need around 1 million nodes.

High performance computing techniques can help towards the resolution of these issues. The addition of a sonic crystal to the launch pad creates more complexity. Sonic crystals gain their peculiar properties from multiple scattering and local resonances effects, which increases the conditioning of BEM matrices.

3.5.1 Solving strategy

Bempp has been chosen to perform the following computations because of its capability to reach higher frequencies. However, both solver show equivalent results. The simulations with the sonic crystal are restricted to a maximum frequency of 200 Hz. Low frequency simulations allow a better understanding of the physical effects and reduce the high frequency BEM issues. The frequency range is set from 20 to 200 Hz with a 20 Hz step. Three materials for the launch pad are analyzed:

1. a rigid medium.
2. a x-y 15×4 sonic crystal with high filling fraction and cylindrical unit cell.
3. a x-y 15×4 sonic crystal with low filling fraction and cylindrical unit cell.

The three configurations are shown in figure (3.7). The simulations are launched over the frequency range for the ignition and lift-off configurations. The iterative GMRES solver is set with a tolerance of 1e-3 and a maximum number of 300 iterations. The computations are launched on a workstation equipped with a 8 cores Intel Xenon E5-2643 CPU at 3.3GHz and 256 GB of RAM.

Once the pressure data on the mesh boundary is solved, the double layer Helmholtz operator \mathcal{K} allows to compute the pressure field on an arbitrary space point. The XY and YZ planes are saved on a grid with a minimum of 20 grid points per wavelength. Similarly, polar data are saved on the XY and YZ planes. The polar data are centered at the origin of the launch pad, namely $(x, y, z) = (0, 0, -3)$, with a radius of 80 m.

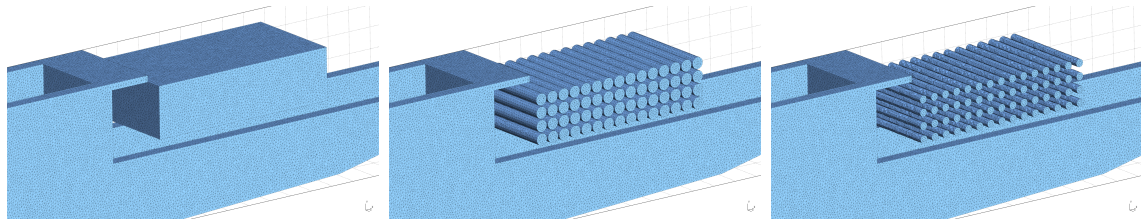


Figure 3.7: 3D view of the noise attenuation media for the Launch Pad. From left to right: Rigid media, sonic crystal with high filling fraction, sonic crystal with low filling fraction. All the media have a width of 8 meters along the z-axis.

We first compute the response of the launch pad without additional medium at 350Hz. The problem has 230k dofs. For the lift-off phase, the assembly of the BEM matrix took 2h45min and the linear system was solved in 3h50min for 82 iterations. The ignition phase needed 5h40 and 120 iterations. 256 Gb of RAM was used. Figure (3.8) shows the resulting pressure field on the XY and YZ planes.

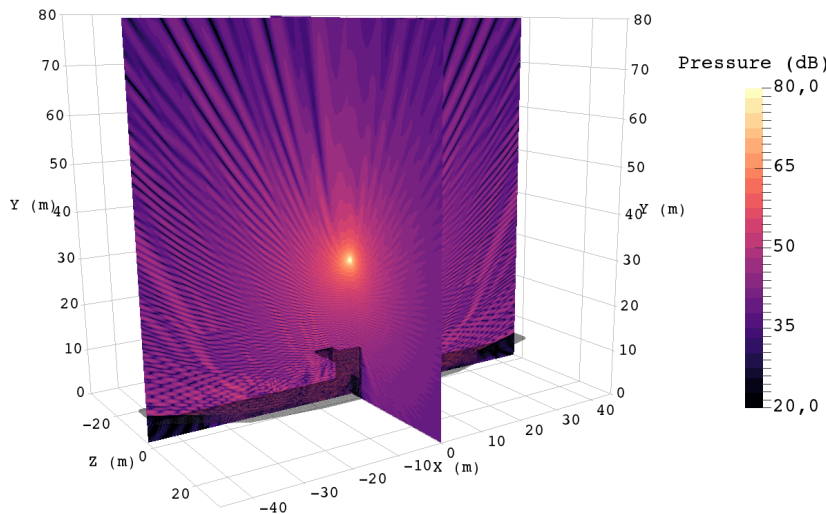


Figure 3.8: Scattering pattern of the Vega launch pad at 350 Hz during liftoff. The total pressure field is in dB.

3.5.2 Sonic crystals: insertion loss for the launch pad

This section illustrates the obtained results with the addition of the sonic crystals and the rigid medium to the launch pad. We define the insertion loss as:

$$\text{IL} = p_{\text{LaunchPad}}^{\text{dB}} - p_{\text{LaunchPad-SC}}^{\text{dB}} \quad (3.25)$$

Here, the insertion loss is defined as the difference in dB between the total pressure field of the launch pad alone and the total pressure field of the launch pad with the sonic crystal. The

insertion loss is a direct measure of the sonic crystal efficiency: a positive value means that the medium reduces the total sound pressure level.

Figure (3.9) shows the insertion loss map at 140Hz on the XY plane around the fairing location. Vega has a height of around 30m. The top of the fairing is located at 41 and 60m for the ignition and lift-off cases, respectively. In the ignition phase, the sonic crystal with high filling fraction has good attenuation properties for the shown frequency. This can be partially explained by the examination of the acoustic field near the sonic crystal. We observe in figure (3.10) that the acoustic transmission is blocked by the crystal in a similar way as done by the rigid medium. This is because the shown frequency lies in the band gap of the high filling fraction sonic crystal. The effect is less pronounced for the low filling fraction case. For the lift-off phase, the effect of the sonic crystal is less clear. Just above the crystal, the maximal values taken by the insertion loss are lower for both sonic crystals, suggesting that the reflecting property of the rigid media is reduced. However, the scattering of the launch pad on its own is complex and the distance between the fairing and the acoustic material is important. It makes it difficult to interpret the results as a consequence of the sonic crystal properties only.

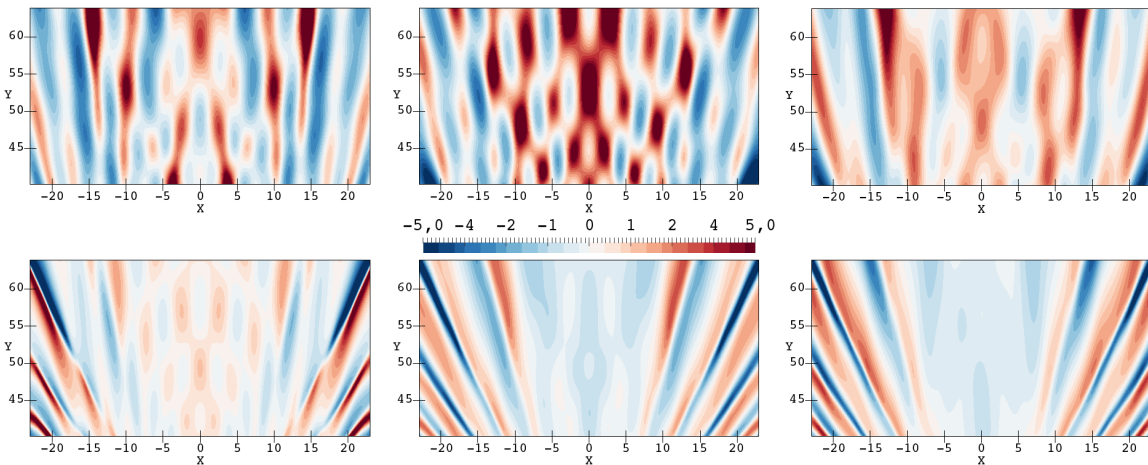


Figure 3.9: Insertion Loss in dB at 140Hz around the rocket fairing for the XY plane. Top: ignition. Bottom: lift-off. From left to right: Rigid media, sonic crystal with high filling fraction, sonic crystal with low filling fraction.

Figure (3.11) shows the total pressure polar field at 140 Hz and the performance of the GMRES solver for the different media. The fairing is located at 90° and there is a positive insertion loss for both the low and high filling fraction sonic crystals at that angle. The polar plot shows that the the sonic crystal scatters the acoustic field in various directions.

The number of iterations clearly increases with the addition of the sonic crystal. Moreover, the \mathcal{H} -matrix assembly for the BEM uses more memory compared to a mesh with an equivalent number of elements without sonic crystal. The multiple scattering effects tend to complexify the problem.

The polar plots can be gathered in the so-called diffusion coefficient. It measures the

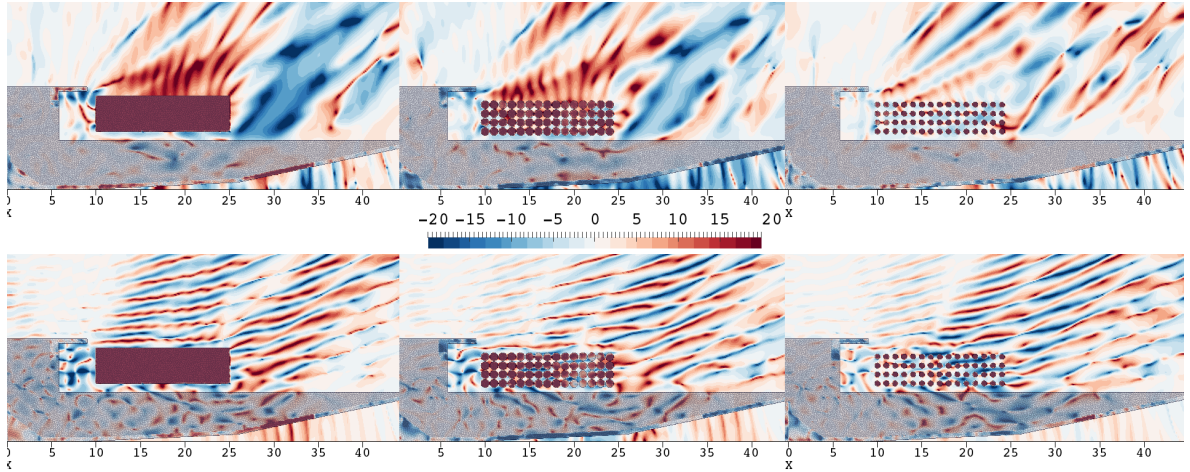
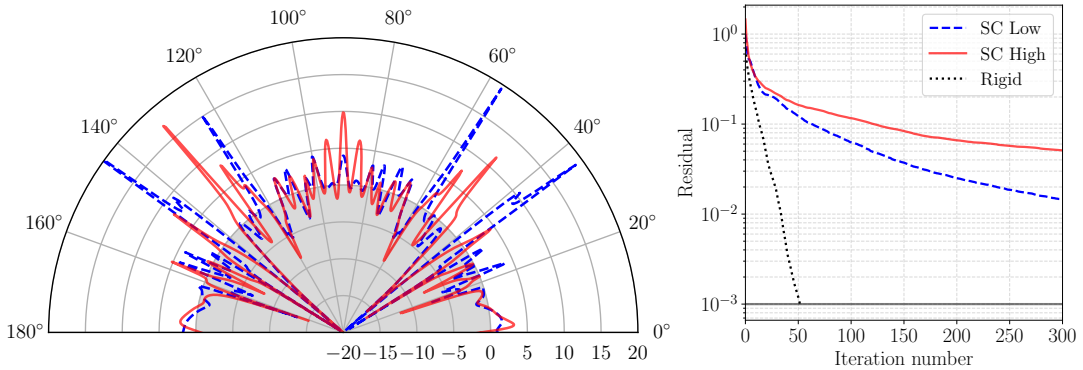


Figure 3.10: Insertion Loss in dB at 140Hz in the near field for the XY plane. Top: ignition. Bottom: lift-off. From left to right: Rigid media, sonic crystal with high filling fraction, sonic crystal with low filling fraction.



(a) Polar plot pressure response in dB for the XY plane. In the grey area, the insertion loss is negative.
(b) GMRES residuals for the different media.

Figure 3.11: Results data at 140Hz for the ignition case with sonic crystal.

spreading of the acoustic field. It is defined by:

$$\delta = \frac{\left(\sum_{i=1}^N 10^{\text{SPL}_i/10} \right)^2 - \sum_{i=1}^N (10^{\text{SPL}_i/10})^2}{(N-1) \sum_{i=1}^N (10^{\text{SPL}_i/10})^2}, \quad (3.26)$$

where SPL_i is the sound pressure level recorded at a fixed angle of subscript i . This coefficient is shown in Figure (3.12) for the ignition case. The diffusion coefficient is shown for the launch pad without and with a sonic crystal. A low value means that the acoustic field is spread into some specific directions. At low frequencies, the low filling fraction sonic crystal shows a higher diffusion coefficient than the high filling fraction case.

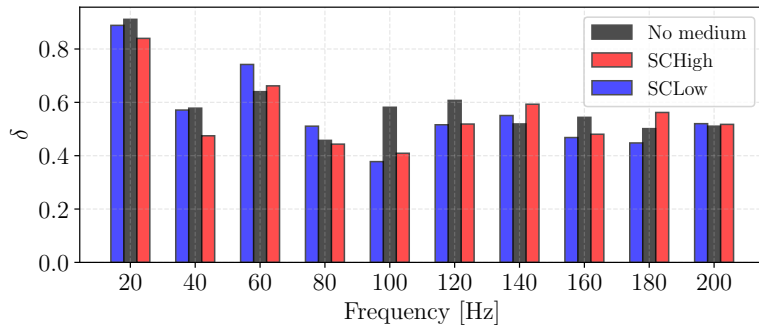


Figure 3.12: Diffusion coefficient of the Vega launch pad during ignition for the XY plane.

3.5.3 Additional remarks

The precedent results have shown that the insertion loss is a complex quantity and that the simulation of such a problem is not without issues. The following points could help to improve the current model:

- The monopole is a great simplification of the rocket source. A more realistic source would be more directional and of high amplitude. However, a source with a realistic amplitude would create high nonlinearities. These nonlinearities can completely change the nature of the acoustic field and the properties of the absorbing materials. For instance, the behaviour of the a Helmholtz resonator at high amplitudes has been studied in [44].
- The next step towards a more realistic simulation could be to use CFD data for the flow close to the exhaust jet and BEM simulations for the far field, as proposed in [45]. A hybrid approach [46] would be interesting but numerically more challenging.
- The current approach could adapt the Green function to take into account the impedance of the ground and the symmetry of the problem.
- Simulations for a sonic crystal with local resonances have been performed in VAOne until 100Hz. The improvement of the BEM preconditioning as well as periodic BEM techniques could help to simulate such complex geometries.
- The frequency approach is not able to catch the time dependent spreading of the reflected acoustic waves by the sonic crystal. This property was studied in [11, 47].

Finally, the insertion loss of the sonic crystal for the launch pad could be improved by tuning the unit cell geometry and the type of periodicity. The locally resonant sonic crystal shows additional attenuation properties, which could be studied more precisely for a 3D application. Moreover, bi-periodic sonic crystals as presented in [47] could further increase the sonic crystal performance. A more precise analysis of the nature of the acoustic field impinging the sonic crystal would help to tune its geometry and periodicity at a smaller scale. A future work could be to study, at a smaller scale, a sonic crystal placed above a reflective sloped ground. This set up could be excited by a monopole placed at different locations.

Conclusion

This study has investigated the potential use of a sonic crystal as an add-on to the Vega launch pad. The physical properties of sonic crystals in one and two dimensions are accurately predicted and provide a background to understand the higher dimensional effects. A sample of the 3D insertion loss is used to examine the behaviour of the crystal. Despite the complex scattering of the launch pad, the diffraction properties of the sonic crystal could be demonstrated.

In the future, the bulk effects of the sonic crystal could be further enhanced with the design of an optimized structure including local resonances. A more realistic physical model with additional symmetry considerations could be studied.

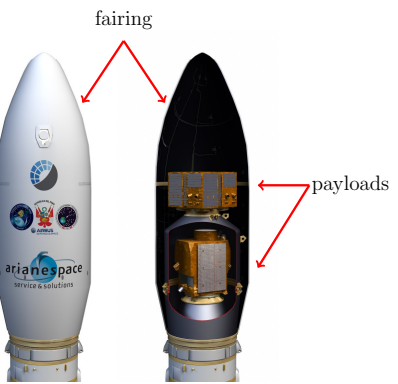
For the encountered Helmholtz problems, mathematical improvements are still needed from a fundamental and numerical point of view. This mathematical and physical duality is essential to improve the prediction of the acoustic field for the complete launch pad.

Appendix A

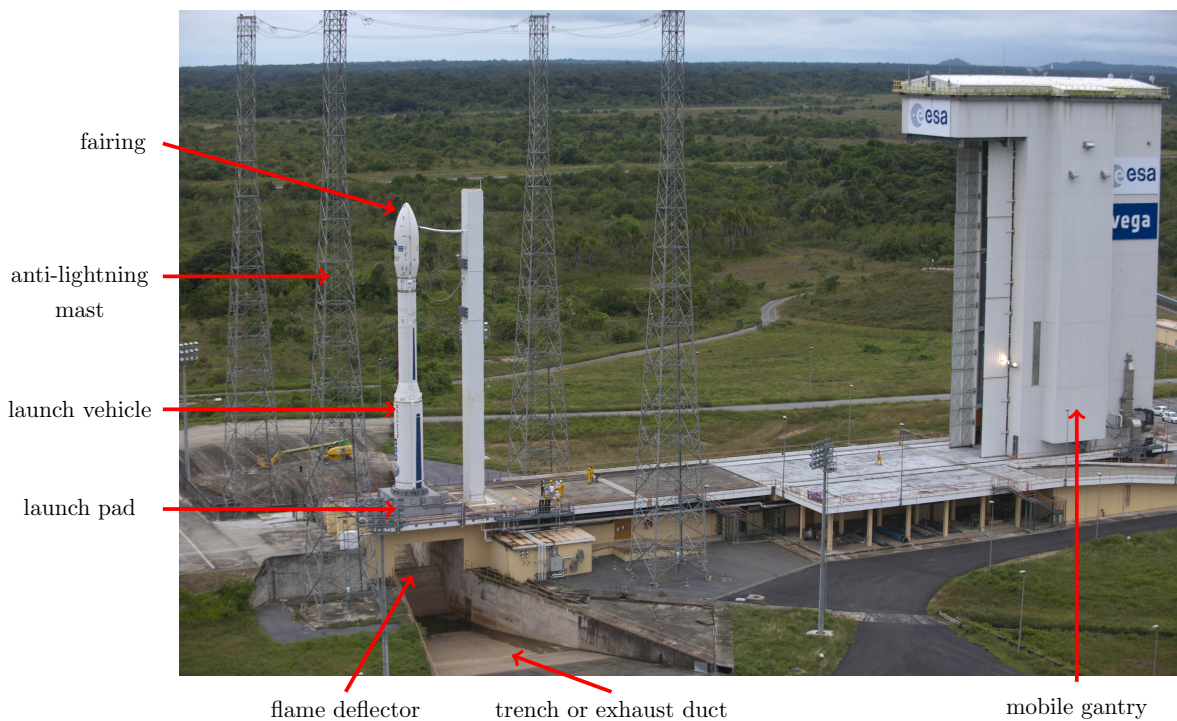
Illustrations of the Vega launcher



(a) Vega during lift-off.



(b) View of the fairing. Source: Arianespace.



(c) Launch platform of Vega.

Appendix B

Locally resonant sonic crystal

This appendix focuses on the behaviour of a locally resonant sonic crystal and a sonic crystal with a more complex geometry. The 2D band gap structure of the locally resonant sonic crystal and its attenuation properties are presented. The differences with the results obtained in section 2.3.1 are highlighted. Finally, the tuning possibility of the band gaps is demonstrated on an unit cell made of 4 resonators.

The locally resonant sonic crystal geometry consists in two embedded circles linked by a tiny opening. We consider the periodic media formed by such a geometry for the square type periodicity. The lattice constant is set to 1, the external radius to 0.45 and the inner radius to 0.4. Figure (B.1a) illustrates a typical mesh of the associated unit cell.

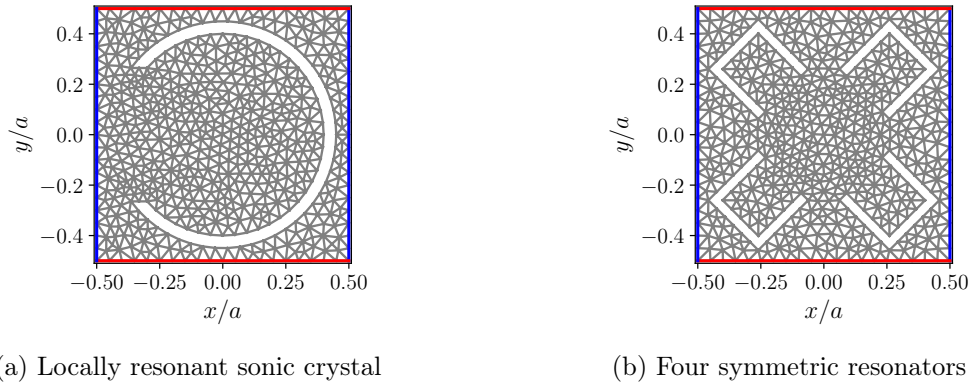


Figure B.1: Mesh examples of the unit cell for finite element discretization. The colored lines illustrate the periodic boundary conditions.

As done in section 2.3.1, we compute the band gap structure of the periodized medium, the Bloch eigenmodes for $(K_x, K_y) = (0, 0)$ and the iso-frequency contours of the diffraction branches. The results are shown in Figure (B.1).

For the locally resonant sonic crystal, there is now two full band gaps at low frequencies:

1. the resonant band gap, which is due to the internal resonance of the scatterer. A simple formula predicts the resonance frequency at 92 Hz. It means that the location of the resonant band gap can be easily tuned. In general, this resonant type band gap is a full band gap.
2. the Bragg band gap, which is of the same nature as for the pure circle case. Both cases share approximately the same upper and lower cutting frequencies.

One might note a loss of symmetry in the iso-frequency contours. If the unit cell geometry loses symmetry properties, the IBZ needs to be extended to properly characterize the media.

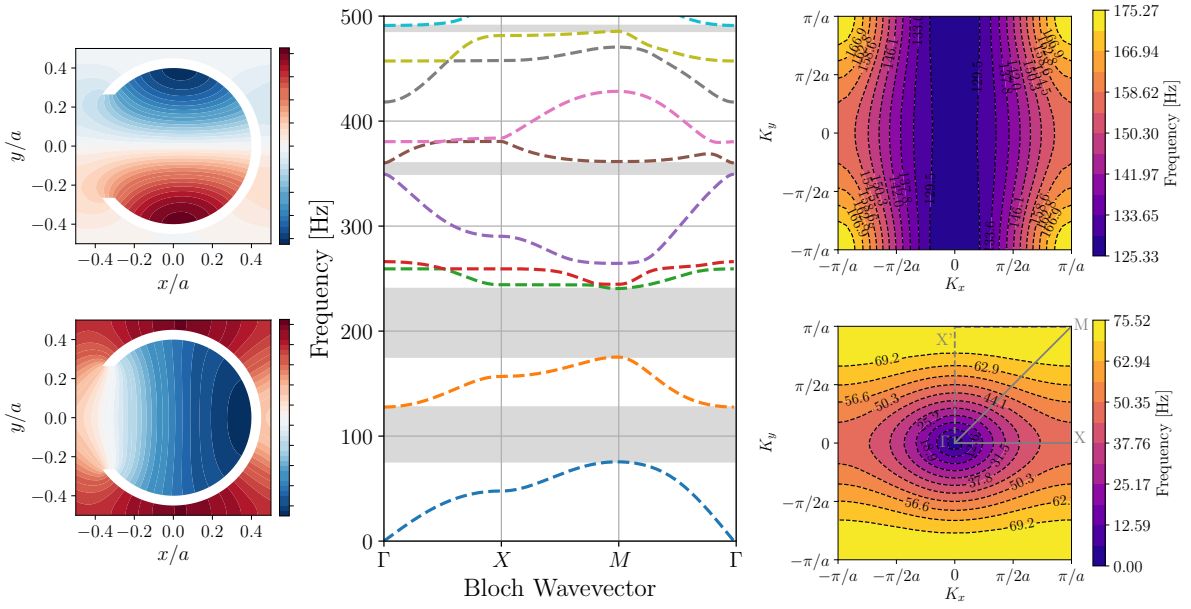


Figure B.2: Physical properties of a locally resonant sonic crystal. Left: Bloch eigenmode 1 (bottom) and 2 (top) for $(K_x, K_y) = (0, 0)$. Middle: Dispersion relation along Γ - X - M . The grey bands enhance the band gaps. Right: Iso-frequency countours of the eigenmode 0 (bottom) and 1 (top).

In this particular case, the dispersion relation should be plotted along Γ - X - M and along Γ - X' - M . This would change the location of the partial band gaps, but it does not change the location of the full band gaps.

The transmission properties of the previous sonic crystal can be analyzed and compared to the pure circle case (cf section 2.3.2 and 2.3.3). The transmission loss for the 1-direction transmission problem is shown in figure (B.3), and the insertion loss of the 2-directions problem is shown in figure (B.4).

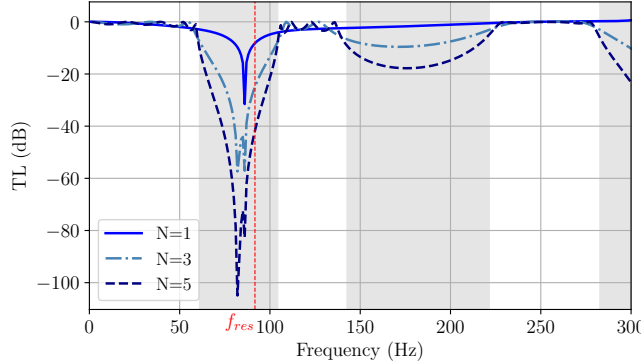


Figure B.3: Transmission loss for a 1-direction finite locally resonant sonic crystal composed of one, three and five layers. The grey areas represent the band gaps in the Γ - X direction.

For the 1-direction transmission problem, there is a pronounced difference in the atten-

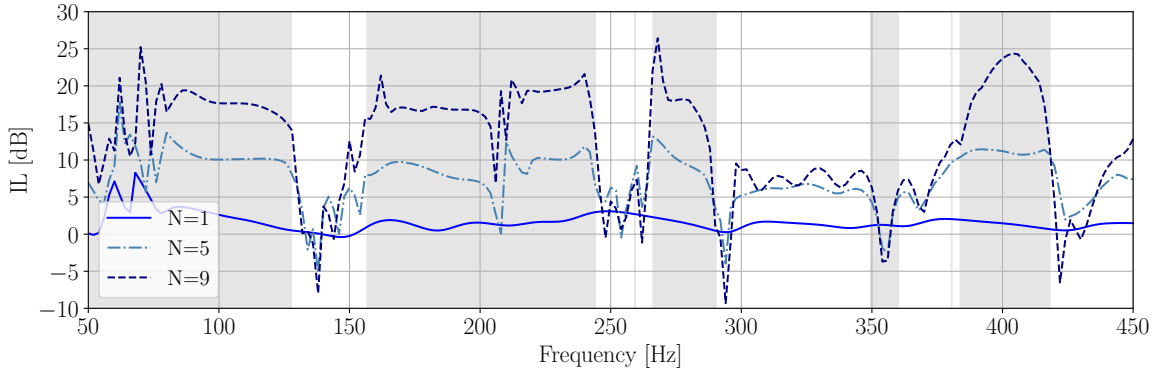


Figure B.4: Integrated Insertion Loss of a 2D finite sonic crystal composed of 5×1 , 5×5 and 5×9 locally resonant unit cells. The grey areas represent the band gaps in the Γ - X direction.

uation mechanism between the resonant and the Bragg band gap. The attenuation in the resonant band gap is stronger than in the Bragg gap. The resonant gap attenuation is localized around a peak, which seems to correspond to the resonance of the system. For the 2-directions transmission problem, there is an increase of the insertion loss inside the gaps with the number of layers in the y-direction. This fact seems to be independent of the band gap nature. Contrary to the 1-direction transmission problem, the attenuation efficiency of the resonant and Bragg band gaps is similar.

Until now, the attenuation has been observed behind the sonic crystal. If one looks at the attenuation in front of the crystal, one can observe a high reflection of the sonic crystal due to the Helmholtz resonance and diffraction gratings.

A further work could study whether the insertion loss measured here represents the actual behaviour of the crystal. Is an average value acceptable to judge the attenuation efficiency ? It might be accurate enough in 2D, but the case becomes more complicated with a 3D crystal. For large applications such as the launch pad, it would be interesting to compute the 2D far field signature of the 2D crystal with for instance a Kirchhoff-Helmholtz integral. The results could be compared with those obtained in section 3.4.

In order to illustrate the tuning possibility of sonic crystals, the band gap structure is computed for a geometry made of four resonators oriented towards the center of the unit cell, as shown in figure B.1b. The results are plotted in figure B.5. For this peculiar geometry, a 100 Hz wide full band gap appears just above 300Hz and the diffraction branches are gathered below this band gap. One might suppose that Bragg and resonant band gaps are coupled in a single, but wider gap. Further analysis is needed to understand if such a band gap is more efficient than isolated band gaps in term of transmission, reflection and insertion loss.

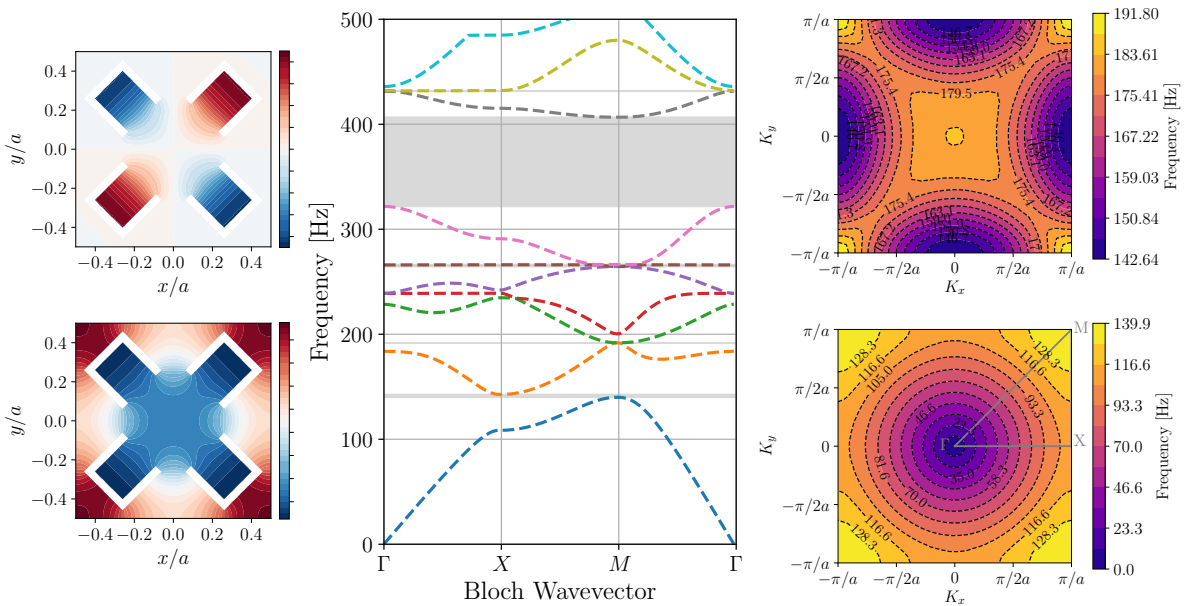


Figure B.5: Physical properties for a set of coupled resonators sonic crystal. Left: Bloch eigenmode 1 (bottom) and 5 (top) for $(K_x, K_y) = (0, 0)$. Middle: Dispersion relation along the IBZ Γ -X- M . The grey bands enhance the band gaps. Right: Iso-frequency countours of the eigenmode 0 (bottom) and 1 (top).

Appendix C

Difficulties for 3D accelerated boundary element method

This appendix summarizes the numerical and computational difficulties encountered for the 3D BEM computations done in chapter 3, especially for the launch pad scattering problem with the addition of the sonic crystal. Both VAOne and Bempp tools are considered.

C.1 High frequency limit

In VAOne, the FMM algorithm is limited to the adimensional wavenumber $kD \approx 500$. Applied to the size of the launch pad ($\approx 100\text{m}$), this condition restricts all the VAOne computations to a maximal frequency of 160 Hz. This pure frequency limitation comes from the implemented FMM algorithm and is explained in [32].

In Bempp, there is no such frequency restriction and the scattering of the launch pad could be run until 350Hz (cf figure (3.8)), which represents around 100 wavelengths along the boundary. In Bempp, the high frequency limitation comes thus from the mesh discretization. The Helmholtz kernel has an oscillatory behaviour: a common rule of thumb is to keep a value of around 6-8 elements per wavelength in order to obtain a reasonable accuracy. The higher the frequency, the finer the mesh and the larger the BEM matrix. In practice, a large BEM matrix leads to a memory limitation. This limitation comes from the \mathcal{H} -matrix compression. Even if this method uses a small amount of memory compared to the classic BEM, storing a low rank representation of the BEM matrix can be too much memory demanding. On the contrary, the VAOne FMM algorithm uses a low amount of memory. This is because the FMM only stores a small part of the BEM matrix, namely the dense part containing the near field interactions. The memory requirements for the FMM depends on the size of the cluster tree.

C.2 Multiple scattering

Multiple scattering was found to be the most critical issue in the computations, because of the complex and unconnected boundaries. As a consequence, the iterative solver shows a poor convergence rate. We now illustrate such an example computed with Bempp.

Let us consider the scattering of the sonic crystal from section 3.4. We report in figure (C.1) the number of GMRES iterations over the frequency range for the two studied cases: the sonic crystal made of 4×5 cylinders and of 4×5 resonant cylinders. The maximum number of iterations is set to 200 and the GMRES tolerance to 1e-5. According to figure (C.1), there is a clear influence of the sonic crystal geometry on the maximum number of iterations.

For the cylinder case, the maximum number of iterations stays reasonable across the

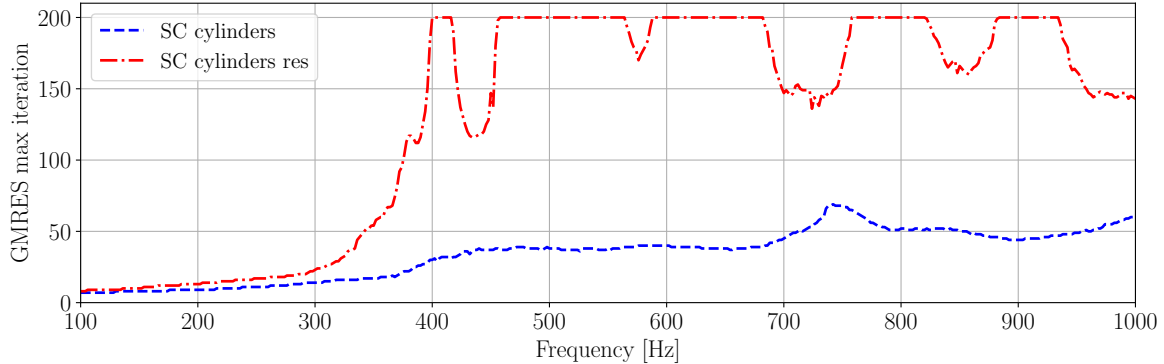


Figure C.1: Number of maximum GMRES iterations for a finite 3D sonic crystal composed of 4×5 unit cells. The cylinders and resonant cylinders cases contain respectively 10 and 15k nodes. To be compared with figure (3.5).

frequency range. Small variations occur for some frequencies. However, the problem becomes critical for the resonant cylinder case. The inner resonances might lead to spurious frequencies. The maximal number of iterations seems to depend on the underlying physical complexity of the sonic crystal.

The problem is more pronounced when the 15×4 sonic crystal is added to the launch pad geometry, as illustrated in figure (3.11). Sonic crystal might have a complex behaviour but it should not affect the efficiency of the numerical method.

However, when equivalent computations are launched in VAOne, it is observed that VAOne needs less iterations to converge compared to Bempp. The difference in the maximal number of iterations is well pronounced for the resonant sonic crystal case. An explanation to this behaviour might be related to the efficiency of the BEM matrix preconditioning.

VAOne uses an ILUT preconditioner whereas Bempp preconditions the BEM matrix by applying the inverse of the mass matrix. To the author's opinion, the ILUT method is more efficient because it acts directly on the BEM matrix, whereas the mass matrix only depends on the basis functions arising from the choice of the boundary elements.

From the above explanations, it is assumed than the sonic crystal increases the conditioning of the BEM matrix. It would then be interesting to implement a $\mathcal{O}(N)$ norm estimate (at most) for the BEM or compressed BEM matrix. A precise analysis of the eigenvalues or of the pseudo-spectra [48] could be attempted for different BEM formulations and preconditioners. However, these propositions might be challenging to apply through fast BEM techniques, since the BEM matrix is partially computed and the possible operations are restricted to matrix-vector products.

Besides the operator preconditioning for the boundary integral equation, the preconditioning of the linear system is critical. Periodic BEM techniques have been proposed in [43] to reduce the computational resources of the presented 4×5 sonic crystal. A future study could attempt to take into account the periodicity of the {launch pad-sonic crystal} geometry and build a Toeplitz structure matrix for this problem.

Finally, it has been observed that the low rank approximation of the BEM matrix becomes less efficient in the presence of complex geometries such as the launch pad with the sonic

crystal.

C.3 Position of the source

According to the numerical experiments on the launch pad, It has been noticed that the position of the acoustic source has an influence on the number of GMRES iterations. For instance, for a fixed mesh and frequency, the ignition case needs more iterations to converge than the lift-off case. If the source is too close to the surface, the number of needed iterations to achieve a reasonable accuracy becomes prohibitive. This constraint might be an important limitation towards the modeling of a more realistic source.

Moreover, additional sources could be added to the launch pad model to take into account the reflection of the ground or geometrical symmetries. It would be interesting to study the performance of the VAOne and Bempp solvers for the launch pad problem with multiple sources.

C.4 Additional remarks

The performance of the GMRES solver was the main issue of this study. In Bempp, different iterative solvers were tried but the GMRES and fGMRES techniques showed the best performance. Further studies could investigate new types of iterative solvers, such as multi-grid methods. Additional solvers features could be a BEM fast frequency sweep or the BEM performance on non-uniform meshes.

A test code can be found on Github to reproduce the discussed behaviours:
<https://github.com/pmarchne/SC> (see the 3D-bempp/SC_Jasa folder)

Bibliography

- [1] Jorge P Arenas and Ravi N Margasahayam. **Noise and vibration of spacecraft structures**. In: *Ingeniare. Revista chilena de ingenieria* 14.3 (2006).
- [2] ESA. **Large European Acoustic Facility (LEAF)**. URL: https://www.esa.int/Our_Activities/Space_Engineering_Technology/Test_centre/Large_European_Acoustic_Facility_LEAF.
- [3] Arianespace. **Ariane 5: User's Manual**. Arianespace, 2016.
- [4] Arianespace. **Vega: User's Manual**. Arianespace, 2014.
- [5] H Defosse and MA Hamdi. **Vibro-acoustic study of Ariane V launcher during lift-off**. In: *INTER-NOISE and NOISE-CON Congress and Conference Proceedings*. Vol. 2000. 4. Institute of Noise Control Engineering. 2000, pp. 3574–3582.
- [6] Jamil Kanfoud et al. **Development of an analytical solution of modified Biot's equations for the optimization of lightweight acoustic protection**. In: *The Journal of the Acoustical Society of America* 125.2 (2009), pp. 863–872.
- [7] Tomoaki Tatsukawa et al. **Multi-Objective Aeroacoustic Design Exploration of Launch-Pad Flame Deflector Using Large-Eddy Simulation**. In: *Journal of Spacecraft and Rockets* (2016), pp. 751–758.
- [8] Jeffrey West et al. **Development of Modeling Capabilities for Launch Pad Acoustics and Ignition Transient Environment Prediction**. In: *18th AIAA/CEAS Aeroacoustics Conference (33rd AIAA Aeroacoustics Conference)*. 2012, p. 2094.
- [9] Max Kandula. **Broadband shock noise reduction in turbulent jets by water injection**. In: *Applied Acoustics* 70.7 (2009), pp. 1009–1014.
- [10] D Gely et al. **Reduction of supersonic jet noise-application to the Ariane 5 launch vehicle**. In: *6th Aeroacoustics Conference and Exhibit*. 2000, p. 2026.
- [11] LM Garcia-Raffi et al. **Broadband reduction of the specular reflections by using sonic crystals: A proof of concept for noise mitigation in aerospace applications**. In: *Aerospace Science and Technology* 73 (2018), pp. 300–308.
- [12] European Space Agency. **Sonic crystals for noise reduction at the launch pad**. Technical Report. contract ITT 1-7094, 2014.
- [13] Trevor Cox and Peter d'Antonio. **Acoustic absorbers and diffusers: theory, design and application**. Crc Press, 2016.
- [14] Martin S. Alnæs et al. **The FEniCS Project Version 1.5**. In: *Archive of Numerical Software* 3.100 (2015). DOI: [10.11588/ans.2015.100.20553](https://doi.org/10.11588/ans.2015.100.20553).
- [15] Anders Logg, Kent-Andre Mardal, Garth N. Wells, et al. **Automated Solution of Differential Equations by the Finite Element Method**. Springer, 2012. ISBN: 978-3-642-23098-1. DOI: [10.1007/978-3-642-23099-8](https://doi.org/10.1007/978-3-642-23099-8).
- [16] FEniCS Project. URL: <https://fenicsproject.org/>.

- [17] Simon Horsley. **Solving problems in wave physics**. 2017. URL: <http://people.exeter.ac.uk/sh481/paradoxes.html>.
- [18] Laetitia Roux. **An Analytical Study of a Periodic Multilayered Medium for Underwater Applications**. In: *AAS2017, Perth, Australia*. 2017.
- [19] Karin Tageman. **Modelling of sound transmission through multilayered elements using the transfer matrix method**. Master's thesis. Chalmers University of Technology, 2013.
- [20] Abdelkrim Khelif and Ali Adibi. **Phononic Crystals: Fundamentals and Applications**. Springer, 2015.
- [21] Vicent Romero García. **On the control of propagating acoustic waves in sonic crystals: analytical, numerical and optimization techniques**. PhD thesis. Universidad Politécnica de Valencia, 2010.
- [22] F Alouges. **Analyse variationnelle des équations aux dérivées partielles**. In: *Cours de l'Ecole Polytechnique, Palaiseau* (2015).
- [23] A. Cebrecos. **Sonic Crystals: Fundamentals, characterization and experimental techniques**. In: *LAUM, Le Mans, France*. 2017.
- [24] Vincent Laude et al. **Evanescence Bloch waves and the complex band structure of phononic crystals**. In: *Physical Review B* 80.9 (2009), p. 092301.
- [25] Vincent Laude et al. **Bloch wave deafness and modal conversion at a phononic crystal boundary**. In: *AIP Advances* 1.4 (2011), p. 041402.
- [26] Ivo Babuška et al. **A generalized finite element method for solving the Helmholtz equation in two dimensions with minimal pollution**. In: *Computer methods in applied mechanics and engineering* 128.3-4 (1995), pp. 325–359.
- [27] Alexandre Lardeau, Jean-Philippe Groby, and Vicente Romero-García. **Broadband transmission loss using the overlap of resonances in 3D sonic crystals**. In: *Crystals* 6.5 (2016), p. 51.
- [28] Zhaoxuan Zhang et al. **Topological design of phononic band gap crystals with sixfold symmetric hexagonal lattice**. In: *Computational Materials Science* 139 (2017), pp. 97–105.
- [29] Steven G Johnson. **Notes on perfectly matched layers (PMLs)**. In: *Lecture notes, Massachusetts Institute of Technology, Massachusetts* 29 (2008).
- [30] Alfredo Bermúdez et al. **An optimal perfectly matched layer with unbounded absorbing function for time-harmonic acoustic scattering problems**. In: *Journal of Computational Physics* 223.2 (2007), pp. 469–488.
- [31] Alfredo Bermúdez et al. **An exact bounded perfectly matched layer for time-harmonic scattering problems**. In: *SIAM Journal on Scientific Computing* 30.1 (2007), pp. 312–338.
- [32] Nail A Gumerov and Ramani Duraiswami. **A broadband fast multipole accelerated boundary element method for the three dimensional Helmholtz equation**. In: *The Journal of the Acoustical Society of America* 125.1 (2009), pp. 191–205.

- [33] **VA One 2014.5 Tutorials Guide.** ESI Group.
- [34] W. Śmigaj et al. **Solving boundary integral problems with BEM++.** In: *ACM Transactions on mathematical software* 41.2 (2015), 6:1–6:40. DOI: [10.1145/2590830](https://doi.org/10.1145/2590830).
- [35] bempp services. URL: <https://bempp.com/>.
- [36] Timo Betcke, Elwin van't Wout, and Pierre Gélat. **Computationally efficient boundary element methods for high-frequency Helmholtz problems in unbounded domains.** In: *Modern Solvers for Helmholtz Problems*. Springer, 2017, pp. 215–243.
- [37] Xavier Antoine and Marion Darbas. **Generalized combined field integral equations for the iterative solution of the three-dimensional Helmholtz equation.** In: *ESAIM: Mathematical Modelling and Numerical Analysis* 41.1 (2007), pp. 147–167.
- [38] C Pechstein. **Special Lecture on Boundary Element Methods.** In: *Lecture Notes. Institute of Computational Mathematics, Johannes Kepler University Linz, Linz* (2013).
- [39] Manfred Kaltenbacher. **Computational Acoustics.** Springer, 2017.
- [40] Rajendra Gunda. **Boundary element acoustics and the fast multipole method (FMM).** In: *Sound and Vibration* 42.3 (2008), p. 12.
- [41] D Brunner et al. **Comparison of the fast multipole method with hierarchical matrices for the Helmholtz-BEM.** In: *Computer Modeling in Engineering & Sciences(CMES)* 58.2 (2010), pp. 131–160.
- [42] Nicolas J Pignier, Ciarán J O'Reilly, and Susann Boij. **A Kirchhoff approximation-based numerical method to compute multiple acoustic scattering of a moving source.** In: *Applied Acoustics* 96 (2015), pp. 108–117.
- [43] Mahmoud Karimi, Paul Croaker, and Nicole Kessissoglou. **Acoustic scattering for 3D multi-directional periodic structures using the boundary element method.** In: *The Journal of the Acoustical Society of America* 141.1 (2017), pp. 313–323.
- [44] F Chevillotte et al. **Analysis of the non-linear behavior of micro-perforated plates using lattice Boltzmann method.** In: *SAPEM, Le Mans, France*. 2017.
- [45] P Lukashin, S Strijhak, and G Shcheglov. **Validation of open source code BEM++ for simulation of acoustic problems.** In: *Proceedings of the Institute for System Programming of the RAS* 29.1 (2017), pp. 39–52.
- [46] Mattia Barbarino et al. **Hybrid BEM/empirical approach for scattering of correlated sources in rocket noise prediction.** In: *Journal of Sound and Vibration* 403 (2017), pp. 90–103.
- [47] Javier Redondo et al. **Sound diffusers based on sonic crystals.** In: *The Journal of the Acoustical Society of America* 134.6 (2013), pp. 4412–4417.
- [48] Jacopo Lanzoni. **Numerical computation of resonances and pseudospectra in acoustic scattering.** PhD thesis. UCL (University College London), 2016.
- [49] Noé Jiménez et al. **Rainbow-trapping absorbers: Broadband, perfect and asymmetric sound absorption by subwavelength panels for transmission problems.** In: *Scientific Reports* 7.1 (2017), p. 13595.

- [50] Noé Jiménez et al. **Metadiffusers: Deep-subwavelength sound diffusers**. In: *Scientific reports* 7.1 (2017), p. 5389.
- [51] P Malbéqui, R Davy, and C Bresson. **Experimental characterization of the acoustics of the future Ariane 6 launch pad**. In: *7th european conference for aeronautics and space sciences*. 2017. DOI: [10.13009/EUCASS2017-38](https://doi.org/10.13009/EUCASS2017-38).
- [52] Jian-Bao Li, Yue-Sheng Wang, and Chuanzeng Zhang. **Tuning of acoustic bandgaps in phononic crystals with Helmholtz resonators**. In: *Journal of Vibration and Acoustics* 135.3 (2013), p. 031015.
- [53] Daniel P Elford. **Band gap formation in acoustically resonant phononic crystals**. PhD thesis. © Daniel Peter Elford, 2010.
- [54] Christophe Geuzaine and Jean-François Remacle. **Gmsh: A 3-D finite element mesh generator with built-in pre-and post-processing facilities**. In: *International journal for numerical methods in engineering* 79.11 (2009), pp. 1309–1331. URL: <http://gmsh.info/>.
- [55] María del Pilar Peiró-Torres et al. **Sonic Crystals acoustic screens with diffusion properties**. In: *Euronoise, Crete, Greece*. 2018.
- [56] Oliver G Ernst and Martin J Gander. **Why it is difficult to solve Helmholtz problems with classical iterative methods**. In: *Numerical analysis of multiscale problems*. Springer, 2012, pp. 325–363.